








Report

Focused-beam X-ray fluorescence and diffraction microtomographies for mineralogical and chemical characterization of unsectioned extraterrestrial samples

Antonio LANZIROTTI ^{1*}, Stephen R. SUTTON ^{1,2}, Matthew NEWVILLE ¹,
Adrian BREARLEY ³, and Oliver TSCHAUNER ⁴

¹Center for Advanced Radiation Sources, The University of Chicago, Argonne, Illinois, USA

²Department of the Geophysical Sciences, The University of Chicago, Argonne, Illinois, USA

³Earth and Planetary Sciences, University of New Mexico, Albuquerque, New Mexico, USA

⁴Department of Geoscience, University of Nevada Las Vegas, Las Vegas, Nevada, USA

*Correspondence

Antonio Lanzirotti, Center for Advanced Radiation Sources, The University of Chicago, Argonne, IL 60439, USA.
Email: lanzirotti@uchicago.edu

(Received 26 September 2023; revision accepted 05 January 2024)

Abstract—This study describes the application of new synchrotron X-ray fluorescence (XRF) and diffraction (XRD) microtomographies for the 3-D visualization of chemical and mineralogical variations in unsectioned extraterrestrial samples. These improved methods have been applied to three compositionally diverse chondritic meteorite samples that were between 300 and 400 μm in diameter, including samples prepared from fragments of the CR2 chondrite LaPaz Icefield (LAP) 02342, H5 chondrite MacAlpine Hills (MAC) 88203, and the CM2 chondrite Murchison. The synchrotron-based XRF and XRD tomographies used are focused-beam techniques that measure the intensities of fluorescent and diffracted X-rays in a sample simultaneously during irradiation by a high-energy microfocused incident X-ray beam. Measured sinograms of the emitted and diffracted intensities were then tomographically reconstructed to generate 2-D slices of XRF and XRD intensity through the sample, with reconstructed pixel resolution of 1–2 μm , defined by the resolution of the focused incident X-ray beam. For sample LAP 02342, primary mineral phases that were visualized in reconstructed slices using these techniques included isolated grains of α -Fe, orthopyroxene, and olivine. For our sample of MAC 88203, XRF/XRD tomography allowed visualization of forsteritic olivine as a primary mineral phase, a vitrified fusion crust at the sample surface, identification of localized Cr-rich spinels at spatial resolutions of several micrometers, and imaging of a plagioclase-rich glassy matrix. In the sample of Murchison, major identifiable phases include clinoenstatite- and olivine-rich chondrules, variable serpentine matrix minerals and small Cr-rich spinels. Most notable in the tomographic analysis of Murchison is the ability to quantitatively distinguish and visualize the complex mixture of serpentine-group minerals and associated tochilinite–cronstedtite intergrowths. These methods provide new opportunities for spatially resolved characterization of sample texture, mineralogy, crystal structure, and chemical state in unsectioned samples. This provides researchers an ability to characterize such samples internally with minimal disruption of sample micro-structures and chemistry, possibly without the need for sample extraction from some types of sampling and capture media.

INTRODUCTION

A major challenge in the study of returned samples from extraterrestrial bodies is unraveling the origin and evolution of the material from measured physical and chemical properties in as pristine a state as possible. Analytical methods applicable to characterize the mineralogy and chemistry of meteorites and from returned samples, including lunar, cometary, and asteroidal and from any future planetary missions, are crucial in unraveling parent body histories. Spatially resolved X-ray-based analytical techniques are particularly well-suited for establishing the texture, mineralogy, crystal structure, and chemical state of such materials and offer the ability to conduct analysis in unsectioned samples, potentially even in situ within sampling media (i.e., particles in aerogel or within small, low-absorption capsules), without need for sample extraction and disruption of sample micro-structures and chemistry. X-ray computed microtomography (CMT) methods that measure X-ray attenuation, using either benchtop or synchrotron sources, have become increasingly utilized techniques for analysis of extraterrestrial samples. While the absorption methods can provide detailed 3-D analysis of the density of structures within materials (Ebel & Rivers, 2007; Eckley & Ketcham, 2022; Zeigler et al., 2022), allowing internal visualization of the size, shape, and texture of component phase and void space, it is generally difficult for absorption CMT to directly provide information regarding crystal structure, for uniquely constraining mineralogy, or major/trace element chemistry.

We describe the use of focused-beam X-ray fluorescence (XRF) and diffraction (XRD) microtomographies in studying such extraterrestrial materials and specifically emphasize development efforts for the application of X-ray microbeam diffraction tomography, as this provides researchers a unique methodology for characterizing mineralogy three-dimensionally in unsectioned samples. The synchrotron-based XRF and XRD tomography methods described here are both focused-beam techniques, where measured intensities of either diffracted X-rays that are transmitted through a sample or fluorescent X-rays (XRF) excited in a sample during irradiation by an incident X-ray beam are tomographically reconstructed. X-ray diffraction tomography, in particular, is not currently a standard technique available to researchers and the few examples available are materials science studies (Alvarez-Murga et al., 2011, 2012; Artioli et al., 2010; Bleuet et al., 2008; Dong et al., 2021; Grant et al., 1993; Possenti et al., 2022). While point microfocused XRD methods are a well-established technique for mineralogical analysis of natural materials (Adcock et al., 2017; Flynn et al., 2009; Gräfe et al., 2014; Kayama et al., 2018; Lange et al., 2010; Lanzirotti et al., 2010; Ma et al., 2012; Miyahara et al., 2013; Tschauner, Ma, Lanzirotti, et al. 2020;

Tschauner, Ma, Newville, et al., 2020; Tschauner et al., 2021; Walker et al., 2009), tomographic imaging of measured diffraction intensities for studying complex multi-component samples is relatively novel. Studies of extraterrestrial materials can significantly benefit from such an approach in that there is often a need to analyze small suites of available samples in as a pristine a state as possible, optimally in an as-received, unsectioned state. Such an approach can provide preliminary data to plan consortia studies, direct quantitative information regarding primary and trace mineralogy and chemistry, the crystal structures of the mineral components, mineralogical and chemical zoning, orientation relationships, crystallographic effects of shock strain, and the distribution and composition of alteration products. To our knowledge, this study is the first where XRD microtomography has been applied to the analysis of extraterrestrial materials. We provide here an overview of how coupled XRF-XRD microtomography techniques can be applied to the analysis of meteoritic samples and discuss development efforts for the application of these techniques specifically in studying unsectioned extraterrestrial samples. Examples of how these techniques have been applied to the study of three meteorite samples are provided.

MATERIALS AND METHODS

Samples

Data are presented from three meteorite samples, a fragment of CR2 chondrite LaPaz Icefield (LAP) 02342,6 (Righter & Satterwhite, 2004; Russell et al., 2005; Wasson & Rubin, 2009), a fragment of H5 chondrite MacAlpine Hills (MAC) 88203,30 (Grossman & Score, 1996; Marlow et al., 1994), and a fragment of Murchison (CM2) meteorite. The LAP 02342 and MAC 88203 samples are from the Antarctic Meteorite Collection curated at the NASA Johnson Space Center. The Murchison sample originates from the Field Museum, Chicago, IL, USA. Each of these samples is described individually below and SEM photomicrographs of the mounted samples are shown in Figure 1:

- *LAP 02342,6 (CR2)*: This sample was utilized primarily to produce a synthetic, multigrain object for technique development purposes. A random fragment was coarsely ground and mixed with epoxy resin to simulate particles suspended in a low-density, amorphous matrix. A consequence of this grinding and mixing will be that measured modal mineral abundances may be biased toward more mechanically robust phases. The solidified, aggregate sample was then mounted to a silica fiber (Figure 1a) and served as an initial data set for helping optimize

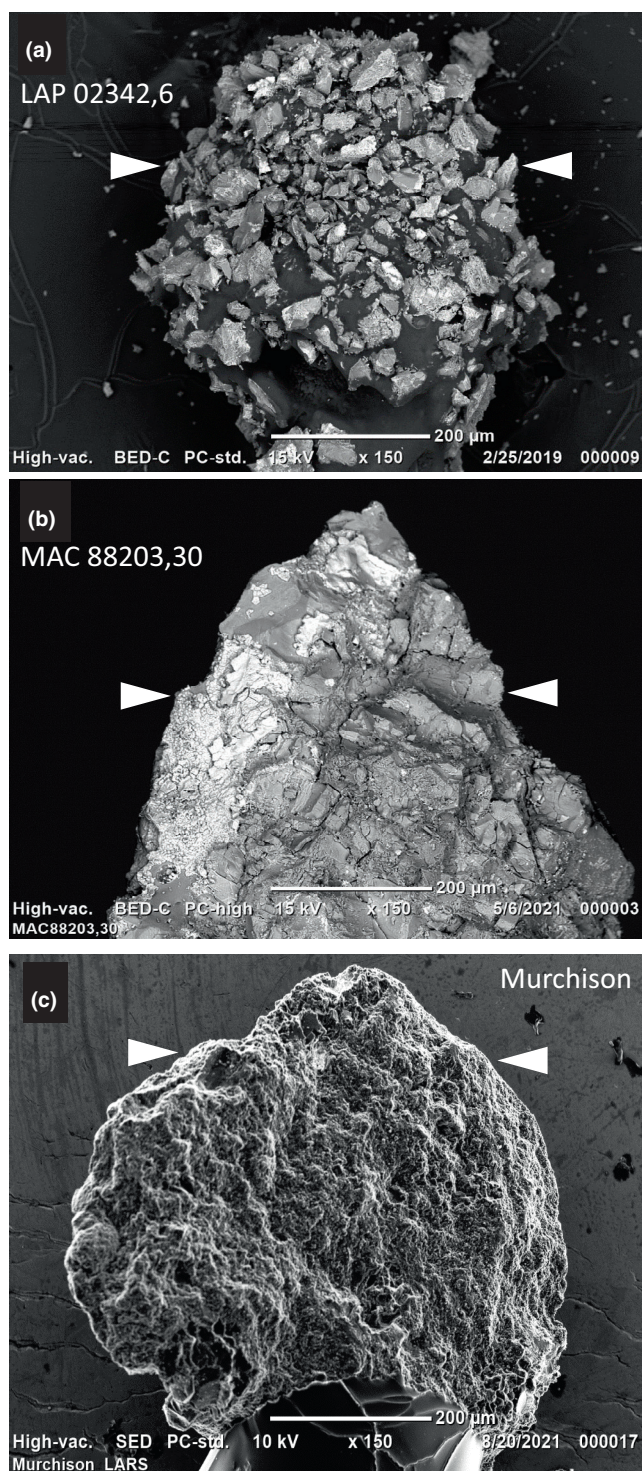


FIGURE 1. Scanning electron photomicrograph of analyzed meteorite fragments: (a) Coarsely ground fragments of CR2 chondrite LAP 02342,6 in epoxy resin and mounted to a silica fiber. (b) Fragment of H5 chondrite MAC 88203,30. (c) Fragment of CM2 chondrite Murchison meteorite mounted to a silica fiber. The triangles show the locations of the planes where tomographic data were collected in each sample.

microdiffraction tomography reconstructions. This sample was $\sim 500 \mu\text{m}$ in diameter at its widest dimension, with tomographic data collected within a plane through a section of sample that was $\sim 420 \mu\text{m}$ in diameter (designated by the two triangles in Figure 1a).

- *MAC 88203 (H5)*: This sample is an intact, $\sim 500\text{-}\mu\text{m}$ -diameter meteorite pebble collected in Antarctica that was epoxy mounted whole to a silica fiber for tomographic analyses, with tomographic data collected through a section of sample that was $\sim 300 \mu\text{m}$ in diameter (designated by the triangles in Figure 1b). The sample is described as having few conspicuous visible cracks; weathering is categorized as moderate to severe (stage B/C), with large rust halos visible on some metallic grains and along fractures (Grossman & Score, 1996; Marlow et al., 1994; Weisberg et al., 1993).
- *Murchison (CM2)*: This solid, random, $\sim 600\text{-}\mu\text{m}$ -diameter fragment was epoxy mounted to a silica fiber for tomographic analysis. The triangles in Figure 1c designate the $\sim 350\text{-}\mu\text{m}$ -diameter section through the upper portion of this sample which was the target for tomographic analysis.

Synchrotron X-Ray Microtomography Methods

This work used the GSECARS X-ray microprobe at Sector 13 (13-ID-E) at the Advanced Photon Source (APS), Argonne National Laboratory. The 13-ID-E station uses microfocusing mirrors in a Kirkpatrick–Baez (KB) geometry to produce focused X-ray beams as small as $1 \text{ (V)} \times 2 \text{ (H)} \mu\text{m}$ (Sutton et al., 2017), which was the focused spot size used in these experiments. The 3.6-cm period undulator and monochromator allow for a focused monochromatic beam with energies between 2.4 and 28 keV. The double crystal monochromator is cryogenically cooled and can utilize either Si(111) or Si(311) crystals. The monochromator has fixed offset and has no significant energy drift ($<0.05 \text{ eV}$), and continuous monitoring of energy calibration is typically unnecessary. For the experiments described here, the Si(111) crystal set was used, with an intrinsic energy resolution $\Delta E/E = 1.1 \times 10^{-4}$. An incident beam energy of 16.0 keV ($\lambda = 0.7749 \text{ \AA}$) was used for XRF/XRD tomography of sample LAP 02342 (with an incident flux to the sample (I_0) of $\sim 6.9 \times 10^{10} \text{ photons s}^{-1}$), while 18.1 keV ($\lambda = 0.6848 \text{ \AA}$) and 18.0 keV ($\lambda = 0.6888 \text{ \AA}$) were used for the analysis of MAC 88203 (with an incident flux to the sample [I_0] of $\sim 4 \times 10^{12} \text{ photons s}^{-1}$) and Murchison (with an incident flux to the sample [I_0] of $\sim 8.4 \times 10^{11} \text{ photons s}^{-1}$), respectively. The I_0 is measured in a helium-filled, 200-mm-long ion chamber just upstream of

the KB mirror optics. The fiber-mounted samples were placed in a motorized goniometer assembly, which allows for precise centering of the sample relative to the rotation axis (ω). Estimates for radiation dose delivered to each sample in each of the analyzed tomographic slices are 9.4×10^8 Gray (Gy) for LAP 02342, 5.6×10^8 Gy for MAC 88203, and 1.1×10^8 Gy for Murchison.

Motorized stages allow for high precision translation of the sample perpendicular (x), parallel (z), vertically (y) to the incident beam direction, as well as providing rotation of the sample (ω) relative to its adjusted axial center (Figure 2). An optical video microscope for sample observation sits at 45° to the incident beam, an energy-dispersive fluorescence detector at 90° to the incident beam (within the horizontal plane of the synchrotron for polarization reasons), and an area detector sits in transmission geometry oriented normal to the incident beam for XRD measurements downstream of the sample. Energy-dispersive XRF spectra were collected using a Canberra/Mirion SX7, 7-element silicon drift diode detector. Pulse processing for the SX-7 was done with a high-speed Quantum Xpress3 digital spectrometer system. Energy resolution for Mn $K\alpha$ (summed 7-element counts, FWHM) is ~ 130 eV at moderate count rates for the 13-ID-E microprobe. The XRD data were collected using Dectris hybrid-photon-counting detectors, an Eiger X 500 K (active area of 38.6×77.0 mm² with 1030×514 pixels) and an Eiger 2X 1 M (active area of 77.1×79.7 mm² with 1028×1062 pixel) for the other two samples. These systems provide for data collection at frame rates of ~ 1 kHz with pixel sizes of 75 μ m. At the incident beam energies used here, the sample detector distance of ~ 80 mm and detector X-Y positioning provided 2θ coverage between ~ 5.5 – 46° (d -spacings between ~ 0.9 and 7.2 Å) at 18 keV for the Eiger 2X 1M and ~ 7 – 40° (d -spacings between ~ 1.1 and 6.3 Å) for the Eiger X 500 K at 16 keV. Area detector calibrations were done using the Dioptas software (Prescher & Prakapenka, 2015) based on measured powder patterns from CeO₂, a NIST powder diffraction line profile standard. At these conditions, XRD peaks for CeO₂ with d -spacings of ~ 1.0 Å yield FWHM of 0.01 Å, while peaks with d -spacings of ~ 3.1 Å yield FWHM of 0.02 Å. For tomographic XRD, the sample thickness also introduces uncertainties in the derived d -spacings since diffracting grains along the incident beam path are at different sample detector distances. This uncertainty was evaluated empirically using powdered CeO₂ measured at 18 keV incident beam energy. When sample detector distance is varied by 350 μ m, the average thickness of the meteoritic samples analyzed here, calculated peak centroids will vary by up to 0.015 Å at a 2θ angle of $\sim 12.7^\circ$. At a 2θ angle of $\sim 44.3^\circ$ calculated peak centroids will vary by up to 0.002 Å. Taken together, we estimated that the

calculated uncertainties in measured d -spacing are likely $\sim 1\%$.

More conventional full-field computed microtomography experiments, which measure X-ray attenuation through a sample, are generally configured to collect a series of radiographs as a function of angular positions (ω) using an incident X-ray beam large enough to illuminate a large areal extent of the sample. The radiograph is then imaged using either an X-ray sensitive phosphor (which is then imaged optically) or an X-ray sensitive area detector. In these full-field studies, each single radiograph for reconstruction contains both horizontal (x) and vertical (y) positional data with resolution largely defined by the pixel resolution of the sensor, accounting for any magnification of the image. Tomographic reconstruction algorithms are then used to reconstruct a 3-D image of the X-ray attenuation through the sample based on sinograms of pixel position on the sensor versus rotational angle.

By contrast, XRD/XRF microtomography is a 2-D mapping method that uses a focused X-ray microbeam to collect point focused XRD and XRF data as the sample is scanned bidirectionally, using rotation (ω) and translation (x) axes in this case, through the focused incident beam (Figure 2). A pencil-beam approach is required for spatially resolved reconstruction of XRF and diffraction, with the resolution primarily limited by the diameter of the focused beam through the sample. A hybrid pixel area detector is used here to collect the diffracted XRD patterns transmitted through the sample. An energy-dispersive detector is used to also collect XRF spectra emitted from the excited material simultaneously for comparison and to aid in the tomographic reconstruction of the XRD data. These are collected at each x - ω position and are used to define a set of data sinograms based on either azimuthal integrated diffraction intensity (see [Data Reduction and Tomographic Reconstruction Methods](#)) or measured fluorescence intensities at each analysis point. These sinograms can then be used to tomographically reconstruct 2-D slices of the intensity through the sample. The pixel resolution of the reconstruction is defined by the resolution of the focused incident X-ray beam. To construct 3-D images, these analyses would need to incorporate a vertical translation of the sample (y) as well. In these experiments, detector acquisition was triggered by the translational x stage which was scanned continuously as the fast axis for mapping the sinograms (ω as the slow axis). Here, the pixel resolution for the x translation was kept to 1 μ m, which provided some degree of oversampling using a 2 - μ m-diameter focused beam. The x position is scanned continuously and the accumulated XRD and XRF data are binned after every 1 μ m of travel (accumulation times per pixel are between

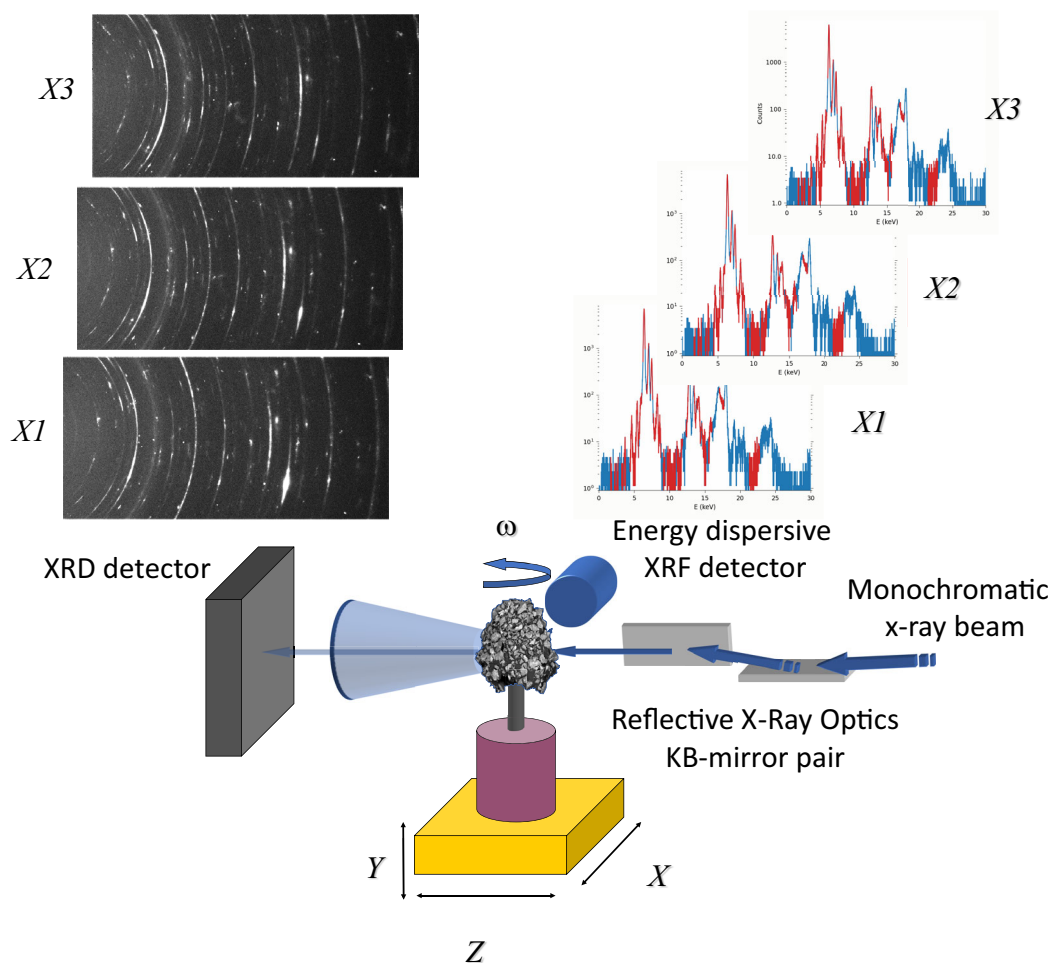


FIGURE 2. Schematic drawing of the synchrotron microbeam XRF-XRD tomography instrumental configuration as used at GSECARS beamline 13-ID-E at the APS. A monochromatic X-ray beam (left) is focused to $\sim 1 \times 2 \mu\text{m}$ ($V \times H$), using Kirkpatrick–Baez microfocusing mirrors, on to an unsectioned sample that is epoxy mounted to a silica fiber. A motorized goniometer assembly allows for precise centering of the sample relative to the rotation axis (ω), with motorized linear stages for high precision translation of the sample perpendicular (x), parallel (z), vertically (y) to the incident beam direction. The X-ray fluorescence signal is measured using a silicon drift diode energy-dispersive detector perpendicular to the beam direction and X-ray diffraction using a pixel array detector downstream of the sample in a transmission geometry. Also shown are three representative, sequential single pixel XRD images (upper left) and XRF spectra (upper right) from the analysis of the Murchison fragment. The XRF and XRD data are collected simultaneously as the x direction is scanned continuously at a rate of $1 \mu\text{m}/25 \text{ ms}$.

20 and 50 ms). For reference, Figure 2 shows three representative single pixel XRD frames and energy-dispersive XRF spectra collected sequentially during the analysis of the Murchison fragment. Both the XRD and XRF data shown were collected using an accumulation time of 25 ms. The ω rotation was set to $\sim 0.5^\circ$ increments for all analyses to ensure that the reconstructed pixel resolution is similar to that of the focused spot size.

Since an energy-dispersive detector is used to measure fluorescence, emissions from multiple elements are obtained simultaneously. However, XRF emission energies $< 16 \text{ keV}$ can be strongly self-absorbed by some

of the samples analyzed here given their average X-ray attenuation for the analyzed thickness. This self-absorption limits our ability to visualize the XRF data deeply within the sample to correlate with the reconstructed XRD data. Our use of full 360° rotations in the tomographic analysis presented here means that the largest degree of attenuation occurs at $\frac{1}{2}$ the sample thickness, at the rotation center. For the micro-XRD tomography, the diffracted X-rays will be the same energy as the incident beam, in this case 18 keV, so that attenuation effects are generally not as pronounced at the sample thicknesses used here. For example, considering a

generalized carbonaceous chondrite with composition and density similar to Murchison, one attenuation length (where the X-ray intensity drops to $1/e$ due to sample absorption) for X-rays at 18 keV would be ~ 500 μm , for X-rays with energies between 4.5 and 9 keV (Ti $K\alpha$ to Zn $K\alpha$) ~ 40 to 70 μm , and at 3.7 keV (Ca $K\alpha$) ~ 20 μm . Tomographic reconstruction of fluorescence intensities at a few attenuation lengths is feasible, but for attenuation lengths approaching 10, accurate reconstruction is unrealistic. Fluorescence at energies below 2 keV (i.e., Al or Si $K\alpha$) in these materials is generally not able to be visualized tomographically due to absorption effects from the sample and from environmental components in the sample to detector path.

Additionally, traditional absorption-contrast tomography relies on the fact that the X-ray attenuation coefficient for a pixel within the sample is independent of the angular orientation of the sample. For fluorescence-contrast tomography, the absorption and subsequent fluorescence probabilities for a pixel within the sample are also independent of the angular orientation of the sample, but the measured intensity of fluorescence energy will be attenuated by the rest of the sample in a manner that depends on the compositional variation in the sample along the path to the detector (self-absorption). For diffraction-contrast tomography, the scattered intensity at a particular scattering angle for a pixel within the sample will depend on its angular orientation unless the sample in that pixel is a perfect powder.

Data Reduction and Tomographic Reconstruction Methods

XRD sinograms consist of arrays of 2-D area-detector images collected at each translation (x) and rotation (ω) position. For example, in the analysis of the Murchison fragment, a single XRD sinogram consists of a total of 508,225 individual 1028×1062 pixel images collected with the Eiger 2 1 M area detector. Images were collected at 701 translation (x) positions at a spatial resolution of 1 μm (translation being the fast-scanning motor) and 725 rotations (ω) with an angular resolution of 0.5° . The individual calibrated 2-D area-detector images are then azimuthally integrated to 1-D arrays of 2θ angle versus diffraction intensity (I_{XRD}) at each of the x - ω positions using the PyFAI python library (Ashiotis et al., 2015). From these integrated 1-D patterns, summed 2θ ranges are then extracted to define new sinograms representative of a given crystallographic reflection. XRF data consist of 1-D arrays of full energy-dispersive spectra (intensities in 4096 energy channels) for each x - ω position, with sinograms generated by summing measured intensities over the range of energy channels representative of a specific elemental emission (using

energy windows that are ~ 320 eV wide). Since this approach integrates the azimuthal angle across the detector plane, technically symmetry-equivalent reflections are visualized. For more granular materials, only a subset of symmetry-equivalent reflections may be visible.

For the tomographic reconstructions, we used the TomoPy software package and explored the use of three different reconstruction algorithms (Gürsoy et al., 2014, 2015). TomoPy is callable from the Larch software package, which was used to build and visualize the sinogram data collected at 13-ID-E (Newville, 2013). The Gridrec algorithm (Dowd et al., 1999) is a direct Fourier-based transformation similar to the filtered-back-projection method and provides excellent computational speed for reconstructions, but is more prone to generating artifacts in reconstruction. We also tested two iterative reconstruction methods (see Gürsoy et al., 2014 and references therein), one using the maximum-likelihood expectation maximization (MLEM) algorithm and one using the ordered-subset expectation maximization (OSEM) algorithm. These iterative algorithms are slower but can be better at avoiding reconstruction artifacts.

The XRF tomographic reconstructions use the measured sinograms of fluorescence intensity as a function of x and ω . As discussed, each pixel of XRF data in the sinogram contains 4096 energy bins (from 0.0 to 40.96 keV), which then defines a 3-D volume of fluorescence intensities, $I_{\text{xrf}}(E, x, \omega)$. To reduce the number of energy points that need to be considered during reconstruction, intensities in a given energy range are summed to define a region of interest (ROI) that represents a fluorescence line (i.e., Fe $K\alpha$, Ti $K\alpha$, etc.). These measured intensities are normalized by the incident flux, I_0 , to account for variations in flux during data collection, and then tomographically reconstructed as described above.

As discussed for the XRD data, each pixel in these sinograms contains a measured 2-D area-detector image. For computational efficiency during reconstruction, we first integrated each of the measured images to intensity as function of scattering angle, 2θ , using 2048 angular bins, to generate a 3-D volume of scattering intensities, $I_{\text{xrd}}(2\theta, x, \omega)$. As was done with the XRF data, ROIs representing the angular width of a given crystallographic reflection were then defined, to reduce the data size, and these were then normalized by the incident flux. An important consideration for XRD tomography is that the XRD reconstructions can be particularly prone to artifacts when crystallite sizes approach the size of the incident beam (Artioli et al., 2010; Vamvakeros et al., 2015). Large crystallites in the sample (relative to the focused beam size) may produce very high intensity reflections at particular angles as the sample rotates through the incident beam (Vamvakeros et al., 2015)

TABLE 1. List of key reflections identified.

<i>d</i> -spacing (Å)	Mineral	<i>hkl</i>
<i>LaPaz Icefield (LAP) 02342</i>		
1.16	α-Fe	211
1.43	α-Fe	200
2.02	α-Fe	110
2.49	Forsterite	112
2.85	Enstatite	610
3.14	Enstatite	221
<i>MacAlpine Hills (MAC) 88203</i>		
3.50	Forsterite	111
1.77	Forsterite	222
2.08	Spinel	400
3.19	Oligoclase	002
~2.50	Vitrified fusion crust	
<i>Murchison</i>		
7.2	Cronstedtite	001
2.53	Cronstedtite	111
3.58	Cronstedtite	002
5.4	Tochilinite	002
6.0	Mixed-layer serpentine	001
1.77	Forsterite	222
2.44	Clinoenstatite	221
1.56	Spinel	511

when repeated crystal units satisfy the Bragg condition. These intense reflections in the sinograms can generate line artifacts that will propagate through the reconstruction. This effect can result in both anomalously elevated and diminished background intensities at a given 2θ angle in reconstructed voxels that lie along the artifact. We evaluated approaches for minimizing such artifacts without significantly compromising our ability to conclusively identify the diffracting mineral phase. This evaluation included a comparison between Gridrec transform and iterative reconstruction methods and an evaluation of filtering the measured sinogram intensities before reconstruction. This filtering consisted of clamping the intensity of the sinograms to given percentile values of the measured range of intensities. The results of these evaluations are discussed below with respect to the analysis of LAP 02342 and then applied to the analysis of MAC 88203 and Murchison samples. Table 1 provides a reference list of the calculated XRD *d*-spacings referred to in the results section for each sample analyzed, along with the likely mineral phase and Miller index for the observed reflection.

Electron Microscopy and Chemical Analysis

Following synchrotron tomographic analysis, singly polished epoxy mounts of the fiber-mounted solid fragments of MAC 88203 and Murchison were produced, suitable for analysis using scanning electron microscopy

(SEM). This was accomplished by embedding each fiber-mounted sample in epoxy to form 5-mm-diameter pucks, which were then ground near the top of each sample (opposite the quartz fiber mount) and polished (final polish with 1- μ m diamond paste). Given the small diameter of the fragments analyzed, it was not feasible to prepare polished sections that coincide precisely with the location of the X-ray tomographic slices collected. However, by targeting the upper portion of each mounted sample, the resultant sections should provide a view of each sample in the vicinity of the tomographic slices and with similar mineral distribution. This allowed us to evaluate whether the mineralogy and chemistry determinations using the XRF/XRD tomographic methods are consistent with what is determined using more conventional backscattered electron (BSE) imaging and electron probe energy-dispersive analysis. The BSE images and EDS chemical analyses were obtained with a JEOL Neoscope II JCM-6000 benchtop SEM equipped with a silicon drift detector (SDD) at GSECARS, operating with an accelerating voltage of 15 kV and at high vacuum. EDS spectra were collected in point mode using 60 s live time acquisition, with elemental concentrations calculated from measured characteristic X-ray emissions using the standardless ZAF correction method. Whole section EDS X-ray maps (512×384 for MAC 88203 and 1024×768 for Murchison) were also collected using 5 ms dwell time per pixel.

RESULTS

LAP 02342

Sample LAP 02342 was used to establish analysis and reconstruction protocols for the rest of the study. Figure 3 shows XRF sinograms (top row) for Ca, Cr, Fe, and Ni $K\alpha$ fluorescence. These are arranged, from left to right, on the order of increasing emission energy. The energy dependence of self-absorption is apparent in Figure 3. The sinogram for Ca $K\alpha$ (emission energy of 3.7 keV) shows a significant decrease in intensity to the right, away from the XRF detector, as the fluorescent X-rays emitted by those pixels must travel through the most sample material to reach the energy-dispersive detector. The sinogram for Ni $K\alpha$ (emission energy of 7.5 keV) shows much less self-absorption. Still, with the sample thickness of $\sim 420 \mu\text{m}$, the tomographic reconstruction for Ca $K\alpha$ does not appear to be significantly attenuated when using 360° rotation. XRF tomographic reconstructions are shown using Gridrec (Figure 3 middle row) and using 250 iterations with OSEM (Figure 4 bottom row). The reconstructions of fluorescence signal using both algorithms are similar, with Gridrec having slightly better resolution and with

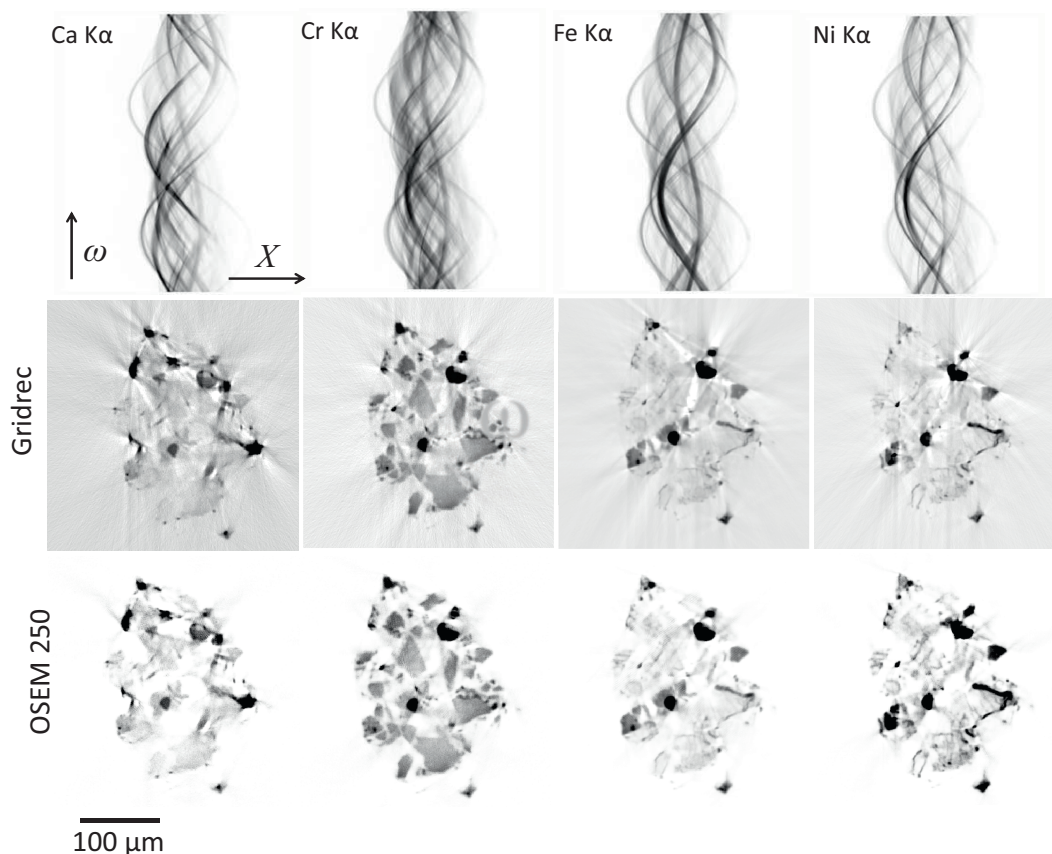


FIGURE 3. XRF sinograms and tomographic reconstructions for sample LAP 02342. For all images, black represents the highest relative intensity and white the lowest relative intensity. Top row: XRF sinograms for Ca, Cr, Fe, and Ni $K\alpha$ fluorescence. Middle row: XRF tomographic reconstructions are using Gridrec algorithm. Bottom row: XRF tomographic reconstructions using OSEM algorithm with 250 iterations.

OSEM reconstructions being less prone to artifacts. The XRF reconstructions clearly delineate individual grains within the epoxy matrix at micron spatial resolutions. Two high-Fe grains, with elevated Ni and Cr, are prominent near the center and the upper right of the reconstructed slices. Scattered grains with elevated Ca and grains with moderate Cr are noted throughout the reconstruction.

In Figure 4, four XRD sinograms (top row) are shown for d -spacings of 4.18, 2.86, 2.51, and 1.43 Å. The sinogram for 4.18 Å (Figure 4, top row, left) does not contain the kind of high-intensity reflections that give artifacts in the reconstruction. By way of contrast, the sinograms for 2.86, 2.51, and 1.43 Å do contain high-intensity reflections and are shown to illustrate how different reconstruction methods and intensity filtering impact the prevalence of artifacts in the reconstruction. This is also useful in evaluating how these artifacts propagate through the integrated 2θ - I_{XRD} in reconstructed voxels.

Reconstructions of the measured 4.18 Å intensities are shown in the first column of Figure 4 using the

Gridrec algorithm on the full range of measured diffraction intensities (Figure 4, Column 1, Row 2), using the OSEM algorithm (with 250 iterations) on the full range of measured diffraction intensities (Column 1, Row 3) and using the Gridrec algorithm after filtering the diffraction intensities to discard intensities outside of 99.9 percentile (Figure 4, Column 1, Row 3). For the XRD reconstructions, the Gridrec and OSEM methods yield similar results, with Gridrec having slightly improved pixel resolution. Additionally, little visible difference is observable using Gridrec with and without pre-reconstruction filtering to a 99.9 percentile distribution. The high-intensity reflections observed at $d = 2.86$, 2.51, and 1.43 Å (Figure 4, Row 1, Columns 2, 3, and 4) generate strong line artifacts during reconstruction with Gridrec on the full range of measured diffraction intensities (Figure 4, Row 3, Columns 2, 3, and 4, with 1σ standard deviation of reconstructed intensities of 35.9, 27.3, and 143.2, respectively), making it difficult to visualize lower intensity reflections from mineral phases. The line artifacts are less pronounced in the OSEM

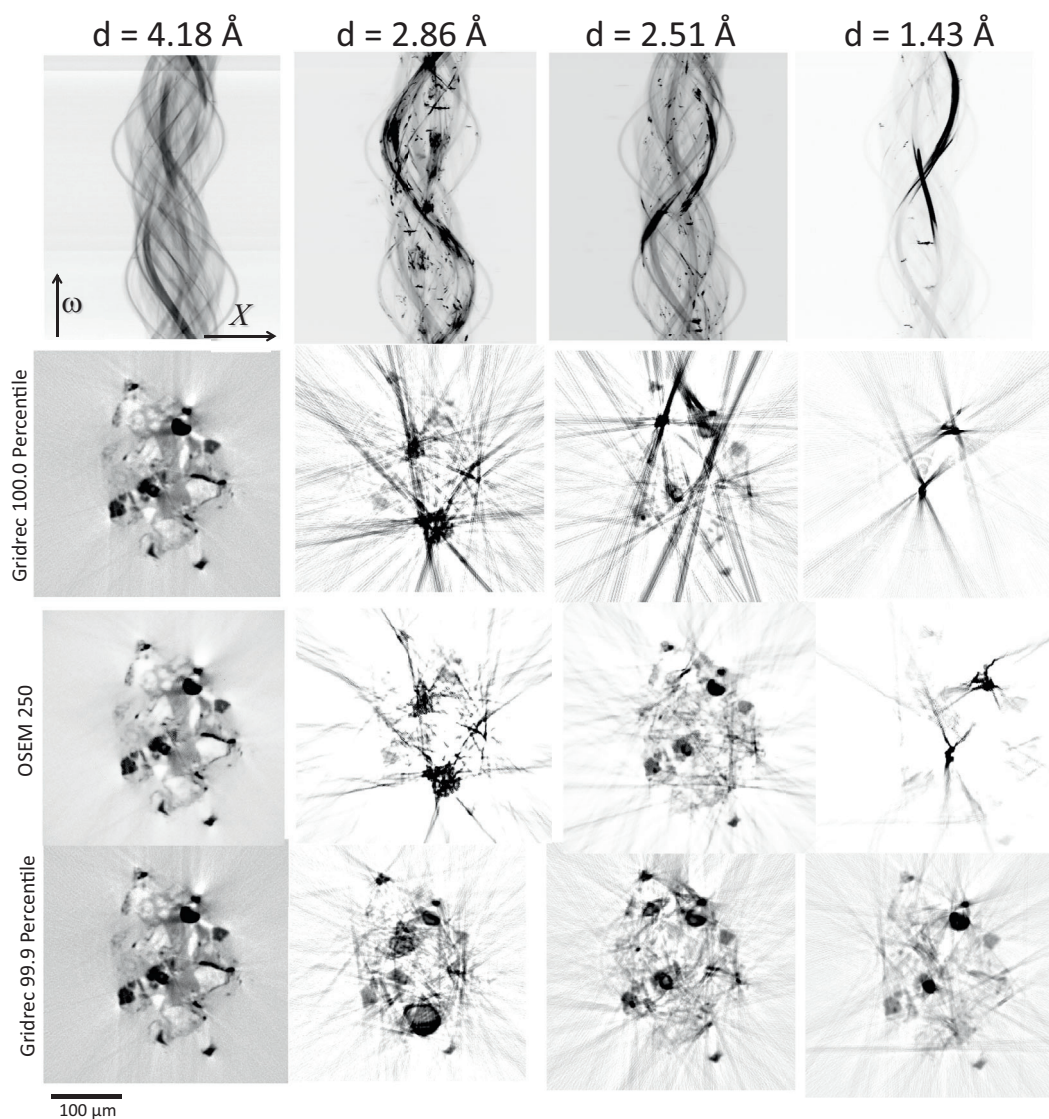


FIGURE 4. XRD sinograms and tomographic reconstructions for sample LAP 02342. For all images, black represents the highest relative intensity and white the lowest relative intensity. First row: XRD sinograms for d -spacings of 4.18, 2.86, 2.51, and 1.43 Å. Second row: reconstructions of the measured diffraction intensities using the Gridrec algorithm on the full range of measured diffraction intensities. Third row: reconstructions using the OSEM algorithm (with 250 iterations) on the full range of measured diffraction intensities. Fourth row: reconstructions using the Gridrec algorithm after filtering the diffraction intensities to discard intensities outside of 99.9 percentile.

reconstructions (Row 4, Columns 2, 3, and 4), particularly that for $d = 2.51$ Å. Line artifacts are even less pronounced for these d -spacings when using filtered Gridrec reconstruction. Figure 4 (Row 4, Columns 2, 3, and 4) shows the reconstructed slice using filtered 99.9 percentile intensities (with 1σ standard deviation of reconstructed intensities of 28.8, 19.7, and 32.3 respectively).

For the XRD tomography, using Gridrec reconstruction of filtered intensities thus appears to provide the best line artifact suppression. We also evaluated the

potential impact of pre-reconstruction filtering on the integrated XRD intensities in reconstructed voxels, crucial for being able to extract qualitatively meaningful phase identification using reconstructed 2θ - I_{XRD} data. Figure 5 shows two ROIs used as part of this evaluation, with the ROIs superimposed over the 4.18 Å reconstruction. For each region, integrated 2θ - I_{XRD} were calculated after tomographic reconstruction over the entire range of measured 2θ 's. The area labeled ROI-1 corresponds to one of the grains identified as having very high Fe fluorescence from the XRF tomographic reconstruction.

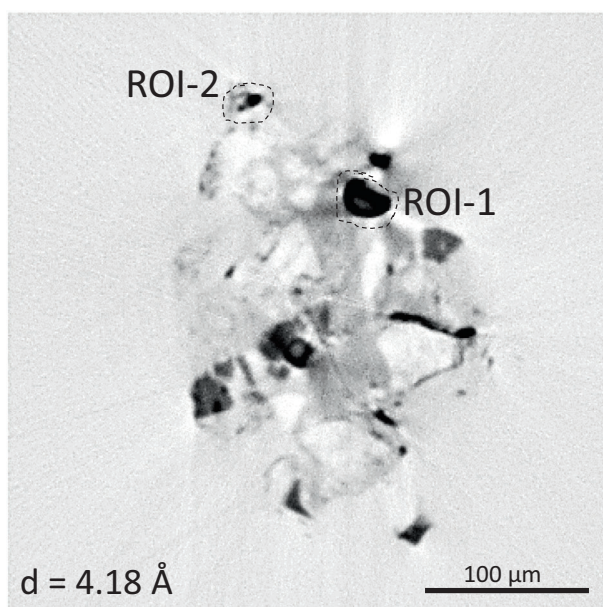


FIGURE 5. XRD tomographic reconstruction for sample LAP 02342 at a d -spacing of 4.177 Å. Superimposed as dashed lines are two regions of interest (ROIs) from which integrated 2θ - I_{XRD} were calculated after tomographic reconstruction.

Figure 6 shows integrated 2θ - I_{XRD} data for the high-Fe area, ROI-1, using 100.0 (i.e., no pre-reconstruction filtering) and 99.9 percentile intensities. Although the calculated filtered and unfiltered $I_{\text{XRD}}(2\theta)$ are similar, there are small differences in relative peak intensities and the high-intensity diffraction peaks in the 99.9 percentile integrations have slightly broader peaks. Also shown is an integrated $I_{\text{XRD}}(2\theta)$ extracted from the original sinogram without reconstruction (labeled Forward Projected Sum). This latter case involves taking the ROI voxels and then forward-projecting them back on to the pixels of the original sinogram. This forward projection allows identification of the areas of the original sinogram data that predominantly contribute to the reconstructed ROI-1 region, which are then used to define a mask for the original sinogram. This sinogram mask is then used with the area-detector images to give the azimuthally integrated Forward Projected Sum 2θ - I_{XRD} data in Figure 6. This summed area detector data are useful for visually evaluating, qualitatively, the relative contribution of mixed mineral phases because differences in relative crystallinity of the individual component phases can be more obvious. For example, contributing phases that have a coarser average crystallite size may produce Debye-Scherrer rings with nonuniform intensity (spotty rings) while finely crystalline components may produce reflections with more uniform intensity and powder-like patterns. The bottom of Figure 6 shows the summed

area-detector image for ROI-1 as a polar transformed projection (“cake” projection of 2θ vs. peak intensity profile). Three relatively smooth high-intensity reflections are visible at 2.02, 1.43, and 1.16 Å. Lower intensity reflections are visible throughout the image, largely as more spotty reflections. These three most intense reflections are all consistent with diffraction from an α -Fe phase. The presence of well-defined, metal-rich chondrules is noted in the petrographic description of LAP 02342 (Righter & Satterwhite, 2004). The smoothness of the three high-intensity reflections in the caked projection shown in Figure 6 also suggest that this metallic Fe phase is very finely crystalline relative to the $\sim 1\text{-}\mu\text{m}$ beam diameter, producing powder-like Debye-Scherrer rings. The lower intensity spotty reflections seen in the caked projection are likely contributed from other mineral phases. In this unreconstructed, summed frame, the sinogram traces for differing phases can overlap and contribute to the 1-D integrated pattern for the forward projected image. However, the examination of the calculated 2θ - I_{XRD} from 100.0 and 99.9 percentile Gridrec tomographic reconstructions show that the contributions from surrounding mineral phases are significantly diminished in the reconstructed patterns. This demonstrates that this method of tomographic reconstruction of XRD intensities is effective in isolating the contributions from mineral phases in geometrically isolated areas of the reconstructed slice, while also being computationally more efficient.

Figure 7 shows similar plots for the ROI-2 area (Figure 5), a grain with significantly lower Fe and Ni fluorescence intensity than the ROI-1 grain. Although the unreconstructed, summed, area-detector image for ROI-2 continues to show a significant intensity contribution from the α -Fe reflections at 2.02, 1.43, and 1.16 Å, in the reconstructed 100.0 and 99.9 percentile 2θ - I_{XRD} integrated patterns these peaks are largely absent. This again demonstrates that pre-reconstruction filtering of the data at 99.9 percentile followed by 1-D azimuthal integration of the Gridrec reconstructed tomographic intensities is effective in isolating the diffracted reflections from the primary mineral phases in the geometrically defined ROI. For ROI-2, the 99.9 percentile reconstructed 2θ - I_{XRD} (Figure 7) shows pronounced reflections at ~ 3.14 and 2.85 Å that are most consistent with enstatite (221) and (610) diffraction lines and a weaker reflection at ~ 2.49 Å most consistent with forsterite (112). The petrographic description of LAP 02342 (Righter & Satterwhite, 2004) notes the presence of abundant pyroxene with compositions ranging from Fs_{1-3} and olivines that range from Fa_{0-5} . All three of these reflections, however, yield moderately discontinuous reflections, consistent with single-crystal type diffraction, so that these phases are likely coarsely crystalline. An

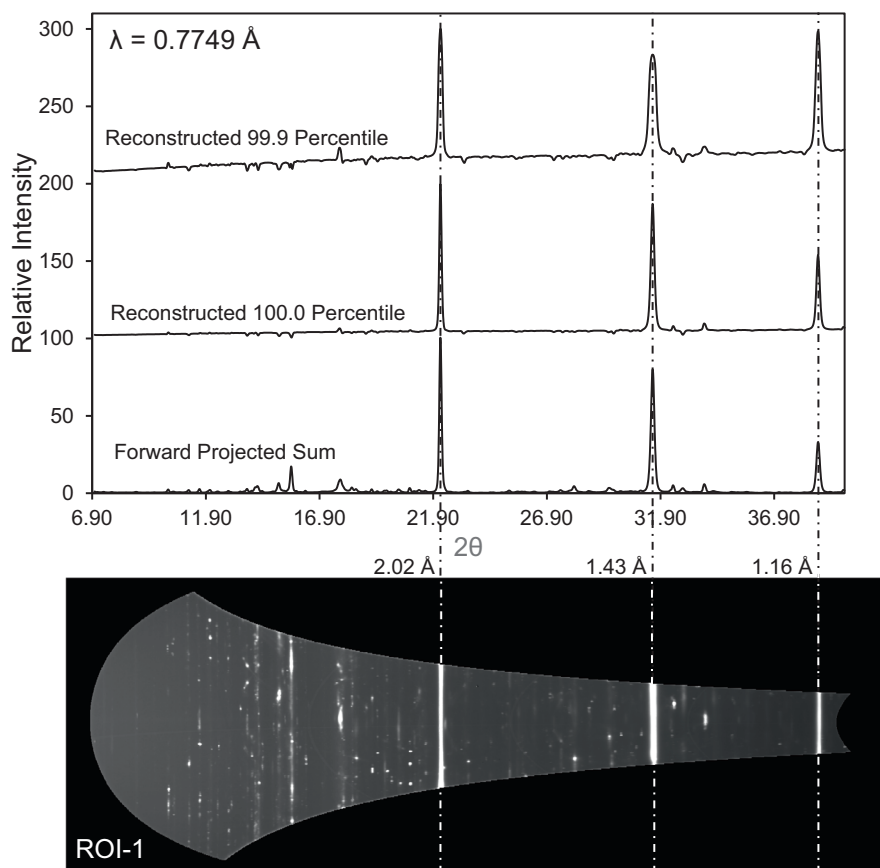


FIGURE 6. Integrated 2θ - I_{XRD} data for LAP 02342 ROI-1 using the reconstructed 100.0 (i.e., no pre-reconstruction filtering) and 99.9 percentile intensities, as well as from the original sinogram without reconstruction (Forward Projected Sum). The forward-projected unreconstructed, summed area-detector image is shown as a caked projection at the bottom of the figure. The dashed (dash-dot) lines show where the relative 2θ position of 2.01, 1.43, and 1.16 Å reflections would lie, reflections likely all diffracted from α -iron.

important consideration for crystalline components such as these that are large, relative to the focused spot size, is that they are likely to be undersampled in the measured diffraction, with integrated peak intensities and widths that are highly variable. This can make unique identification of coarse phases more difficult when using this tomographic technique. It should also be noted that the strong reflection in ROI-2 at 2.85 Å could also be accounted for by diffraction from a calcium-aluminum-rich inclusion (CAI) such as gehlenite that may be present as a minor mineral component in the tomographic slice. This is not definitive, however, given that reflections from enstatite (610) may overlap. Although the occurrence of gehlenite in LAP 02342 would be consistent with the observed presence of CAIs in the petrographic description (Righter & Satterwhite, 2004), such CAI's in CR chondrites are generally rare.

Phyllosilicates were not detected in the XRD tomographic reconstruction of this ground sample of LAP 02342. Le Guillou et al. (2015) found that the

matrix of LAP 02342 is largely composed of relatively MgO-rich phyllosilicates ($\text{Mg}/(\text{Mg} + \text{Fe}) \text{ atom\%} > 0.7$). Compared to the XRD signal from coarser grain phases, phyllosilicates would appear as largely smooth Debye rings and should be discriminable in the diffraction frames. However, given that the fragment was loosely ground and embedded in epoxy in preparation of this sample for tomographic analysis, it is likely that the phyllosilicate grains are not well-preserved after mechanical grinding.

MAC 88203

Unlike sample LAP 02342, sample MAC 88203 consists of a single intact fragment. Figure 8 (top row) shows reconstructed XRF tomograms of Cr, Fe, and Ni $K\alpha$ fluorescence in the MAC 88203 slice. The Ca $K\alpha$ fluorescence reconstruction is not shown here because it is rather strongly self-absorbed, a key difference from the XRF reconstructions of the crushed LAP 02342 sample

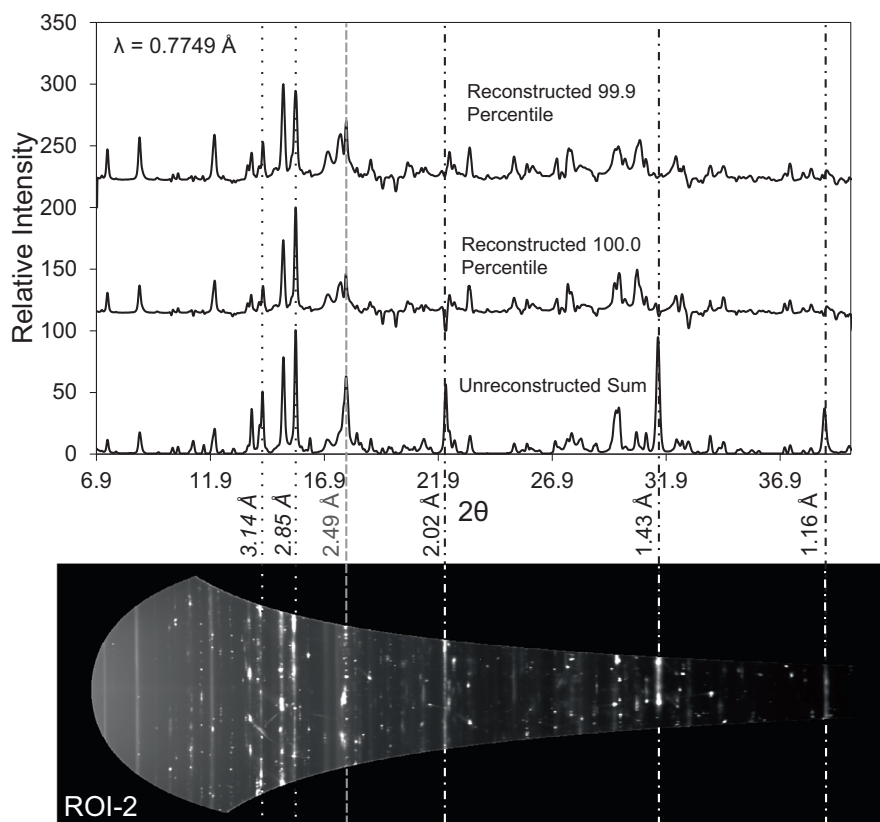


FIGURE 7. Integrated 2θ - I_{XRD} data for LAP 02342 ROI-2 using the reconstructed 100.0 (i.e., no pre-reconstruction filtering) and 99.9 percentile intensities, as well as from the original sinogram without reconstruction (Unreconstructed Sum). The forward-projected unreconstructed, summed area-detector image is also shown as a caked projection at the bottom of the figure. The dashed (dash-dot) lines show relative 2θ position of 2.02, 1.43, and 1.16 Å reflections for α -iron, the dotted lines are at 3.14 and 2.85 Å and are likely from coarsely crystalline enstatite while the dashed gray line is at 2.49 Å is likely from coarsely crystalline olivine.

in an epoxy matrix. In the Fe $K\alpha$ reconstruction, a discontinuous rim of high Fe surrounds the fragment, slightly more notable on the right side of the fragment. Iron fluorescence intensities within the fragment itself are lower than the rim. Approximately 10 isolated subhedral particles are identifiable from the reconstructed Fe $K\alpha$ reconstruction, with fluorescence intensity ~ 3 times lower than what is measured for the rim phases. An example of one of these particles is the region labeled “Particle 1” in Figure 8. These subhedral particles are in turn surrounded by a matrix with approximately half the Fe fluorescence intensity measured in the subhedral particles. The highest Ni fluorescence also occurs as a discontinuous rim at the fragment margins, although more sharply delineated than Fe, and is enriched by up to a factor of 70 compared to the internal fragment and with an Fe/Ni ratio of ~ 6 . The highest Cr is found as small (sub-10 μm diameter) disseminated particles localized in interstitial zones between larger particles.

Reconstructed XRD intensities define phase distributions that closely mirror the XRF reconstructions.

The diffraction is dominated by reflections from two primary mineral phases. The most pronounced diffraction is consistent with olivine of forsteritic composition, largely occurring as a coarsely crystalline phase based on measured area detector data. Tomographic reconstruction of XRD intensity at a d -spacing of 3.50 Å is likely dominated by olivine diffraction (Figure 8, bottom left), with the strongest intensities defining interstitial areas (represented by an ROI labeled “Matrix 1”) between larger subhedral isolated particles (represented by the ROI labeled “Particle 1”). XRD intensities for the subhedral particles in the reconstructed slice are notably lower than the matrix or the fragment rim at all measured 2θ angles. The integrated 99.9 percentile $I_{\text{XRD}}(2\theta)$ for the MAC 88203 fragment are shown in Figure 9 for the entire fragment, the fragment edge, Particle 1, and Matrix 1. Also shown are caked area-detector forward projections for the entire fragment and fragment edge at the bottom of Figure 9. While the area-detector image for the entire fragment is largely defined by spotty diffraction, consistent with diffraction from more coarsely crystalline material, a lower intensity, more

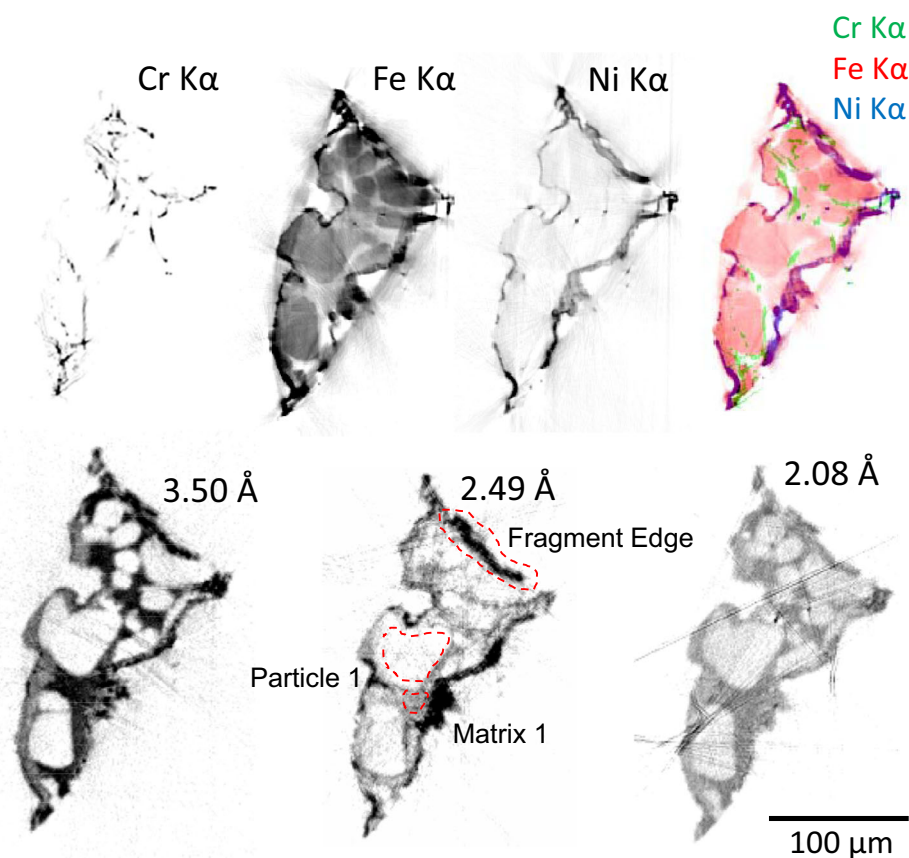


FIGURE 8. Top row: XRF tomographic reconstructions for sample MAC 88203 of Cr, Fe, and Ni $K\alpha$ fluorescence, along with a red-green-blue overlay of all three elements. Bottom row: XRD tomographic reconstruction of diffraction intensity at d -spacings of 3.50, 2.49, and 2.08 Å. Also shown as red dashed areas on the 2.49 Å reconstruction are three regions of interest labeled Matrix 1, Particle 1, and Fragment Edge.

powder-like pattern is superimposed. This component overlaps with the area-detector image from the fragment edge and is visualized by the tomographic reconstruction of diffraction intensity at 2.49 Å (Figure 8, bottom middle). The XRD pattern for the entire fragment is dominated by diffraction from forsteritic olivine. The integrated 2θ - I_{XRD} XRD patterns for the Matrix 1 ROI suggest that forsteritic olivine is the dominant diffracting mineral phase in the matrix as well. Although the integrated 2θ - I_{XRD} for Particle 1 is also consistent with olivine, some reflections that are expected for olivine are of intensity below powder-statistic average and thus not well-defined. Additionally, some negative intensities occur in the reconstructed patterns due to reconstruction artifacts. Both features are a result of crystallite sizes being comparable to the lateral dimensions of the primary X-ray beam. Although these subhedral particles do have moderately elevated Fe fluorescence when compared to the matrix, the reconstructed diffraction data for these subhedral particles have generally lower overall diffraction intensities with discontinuous Debye-Scherrer rings. This may indicate that these particles are more coarsely crystalline relative to the incident beam size.

The reconstructed 2θ - I_{XRD} data of the edge material are primarily defined by a strong, yet diffuse, reflection near 2.5 Å (see Figure 9). The reconstructed diffraction pattern is possibly consistent with either maghemite, which may have formed as a weathering product on the fragment surface, or laihunite, an olivine-group mineral that has been observed to form on interplanetary dust particle surfaces from oxidation of Fe-bearing olivine (Keller et al., 1992). The enrichment in Fe fluorescence for the rim material relative to what is measured in the subhedral particles would be reasonable for maghemite. The description of MAC 88203 notes that the sample exhibits moderate to severe (stage B/C) weathering (Grossman & Score, 1996; Weisberg et al., 1993), which may also be consistent with maghemite. However, an interesting observation from the XRF tomographic reconstruction is that this rim material is also highly enriched in Ni, with an Fe/Ni ratio of ~ 6 . The degree to which terrestrial weathering is likely to lead to Ni enrichment is unclear (Bland et al., 2006).

It is more likely that this edge material represents a thin vitrified fusion crust on the sample; consistent with

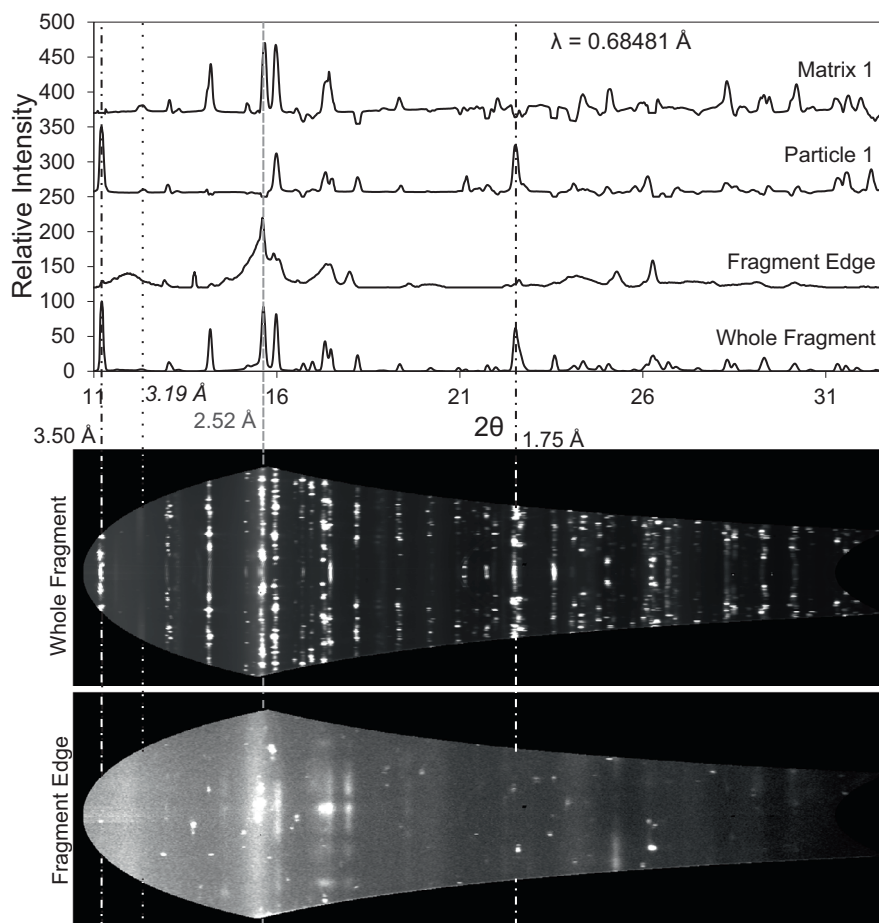


FIGURE 9. Integrated 99.9 percentile 2θ - I_{XRD} data for MAC 88203. Patterns are shown for the Whole Fragment (unreconstructed), and reconstructed patterns for the regions labeled Matrix 1, Particle 1 and Fragment Edge shown in Figure 8. The bottom images show caked area-detector image for the entire fragment and a forward-projected area-detector image for the fragment edge. The dashed (dash-dot) lines show reference positions for high-intensity peaks at 3.50 and 1.77 Å from what is likely forsteritic olivine. The dashed gray line at 2.52 Å denotes position of an observed diffuse reflection that may be from maskelynite. The dotted line defines where the 3.19 Å olivine (002) reflection would be expected.

fusion crusts noted on other stony meteorites that contain numerous olivine phenocrysts set in a glassy mesostasis (Genge et al., 2023). Some studies of fusion crust formation in iron meteorites have identified potential Ni enrichments (El Goresy & Fechtig, 1967), although in stony meteorites the Fe and Ni content of the fusion crust was found to not significantly differ from the composition of the bulk material (Genge & Grady, 1999). The less spotty and more powder-like scattering that is observed is also consistent with the expected poorly crystalline structure of phases in a vitrified fusion crust.

The XRD tomographic reconstruction also shows the presence of less-abundant small particles with elevated diffraction intensity at a d -spacing of 2.08 Å (Figure 8, bottom right) that correlate to small particles with elevated Fe, Cr, and Ni fluorescence in the XRF reconstruction. Unequivocal mineral identification of these small, sub-10 μm particles is difficult given their

small size, their coarse crystallinity (which limits the number of observed reflections), and due to the contribution of diffraction from surrounding olivine. However, the 2.08 Å d -spacing would be consistent with a spinel mineral phase, possibly chromite.

Following initial assessment of the XRF/XRD tomographic reconstruction, the fiber-mounted MAC 88203 fragment was embedded in epoxy to produce a singly polished section for SEM analysis. Figure 10 shows a BSE image (upper left) of this section, along with energy-dispersive maps of Fe, Mg, and Al K-fluorescence. The section is oriented such that it generally correlates to the orientation of the XRF/XRD tomographic slices but is approximately twice the thickness in the horizontal compared to the tomographic slice. The SEM imaging shows that olivine, with an average composition of $\sim\text{Fa}_{27}$, is the dominant mineral component in the section and that a vitrified fusion crust occurs along the right face of the

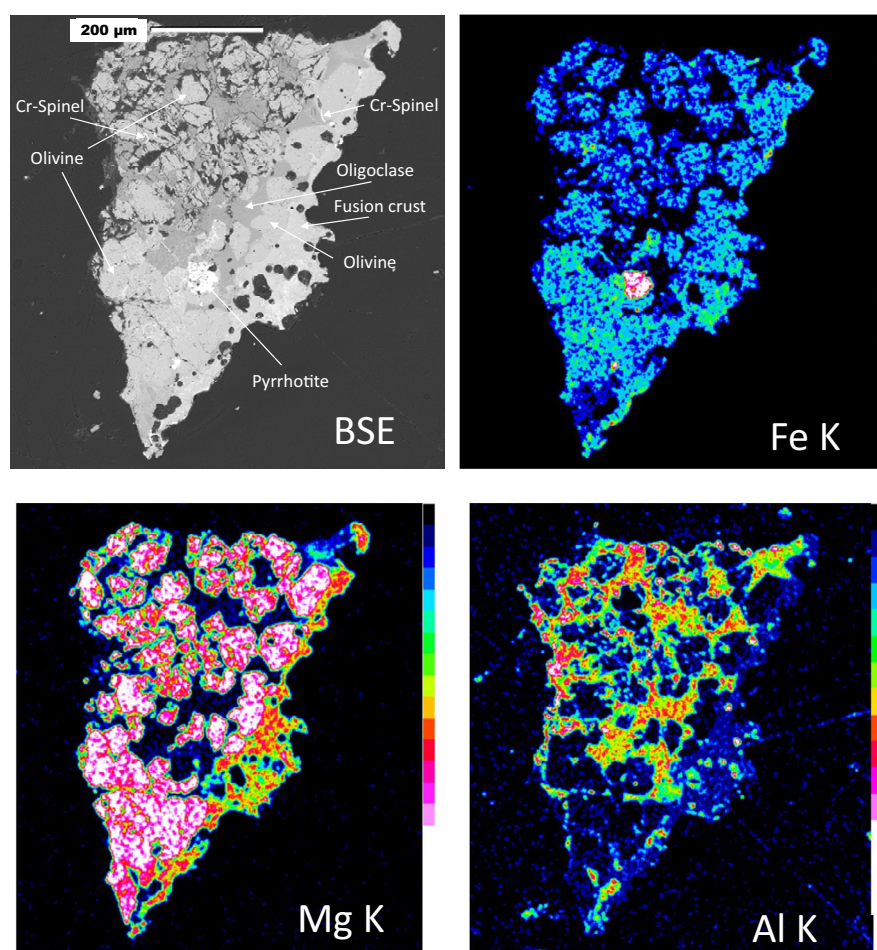


FIGURE 10. BSE image (upper left) and SEM energy-dispersive maps of Fe, Mg, and Al K-fluorescence for epoxy embedded, polished section of sample MAC 88203. Representative phases identified using electron microscopy are noted on the BSE image. Relative fluorescence intensity scales are shown for the energy-dispersive maps.

section. The olivine displays three varying morphologies in the section; notably fractured olivines are found at the upper portion of the section within a matrix of fine-grained oligoclase plagioclase, relatively unfractured olivines occur at the bottom of the section with little interstitial matrix, and notably rounded olivines occur adjacent to the fusion crust to the right of the section. Small iron sulfide and Cr-rich spinel grains are also noted. The prevalence of relatively large, subhedral grains of forsteritic olivine is consistent with the XRF/XRD tomographic imaging. The pronounced fusion crust on one side of the section is also consistent with the interpretations made from the XRF/XRD tomographic analysis. The fusion crust also shows a small enrichment in Fe with SEM EDS mapping (Figure 10, Fe K α map), which was also visualized using XRF tomography (Figure 8). The SEM imaging of the fragment edge does not show detectable iron oxides at the fusion crust, which suggests that the scattering intensities observed for the fragment edge with XRD tomography are

most likely from poorly crystalline, vitrified olivine. Also consistent with the XRF/XRD tomography is the presence of small Cr-rich spinels scattered throughout the fragment matrix. Although a strong reflection from oligoclase is not clearly defined in the matrix from the XRD tomography, both the $I_{\text{XRD}}(2\theta)$ reconstruction of the Matrix 1 ROI for MAC 88203 (Figure 9) and the caked area-detector forward projections for the entire fragment show a weak powder-like reflection at 3.19 Å that would be consistent with the oligoclase (002) reflection. Although the reconstructed XRD patterns for the matrix were most consistent with olivine diffraction, it is possible that the matrix plagioclase is glassy and poorly diffracting, as may be expected of maskelynite.

Murchison

The third example is a ~350- μm -diameter section through a fragment of the Murchison meteorite. The

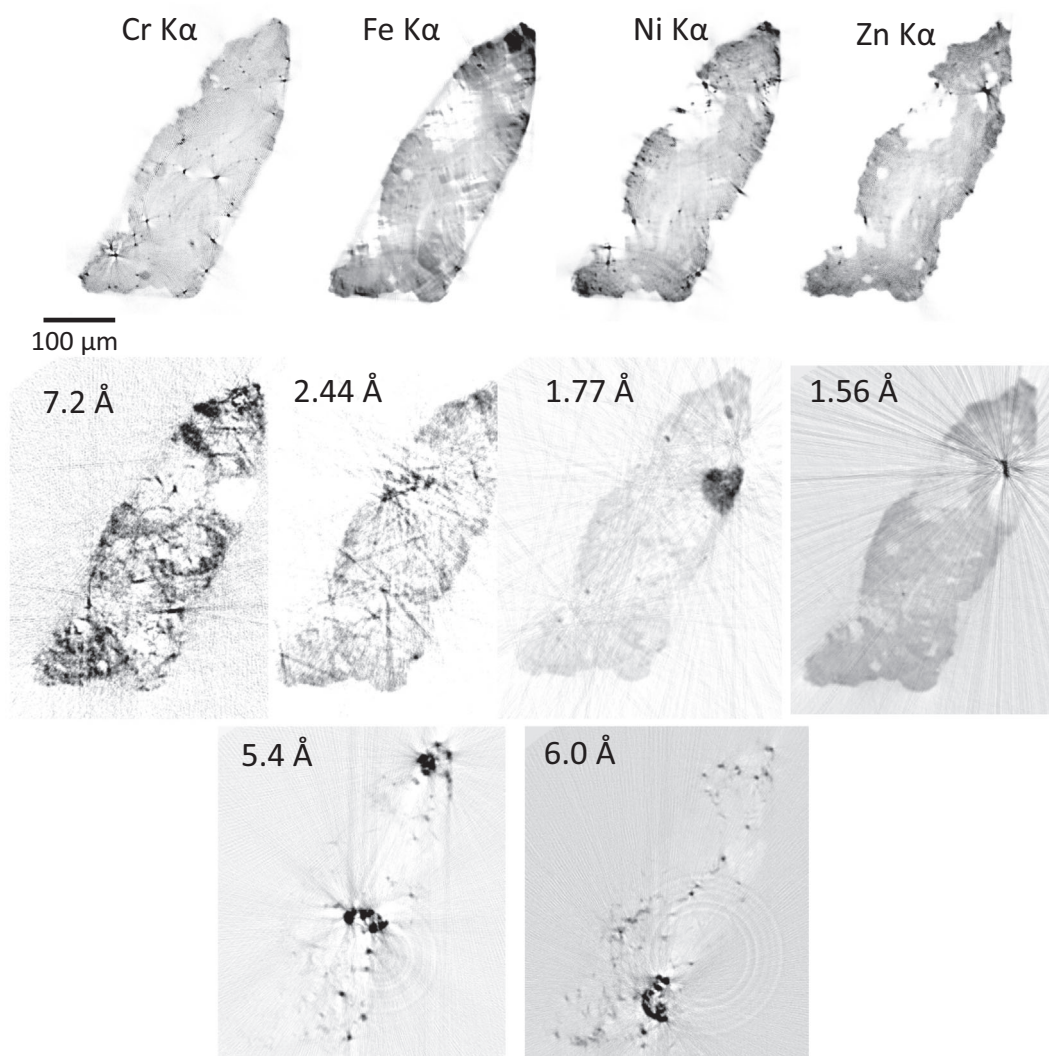


FIGURE 11. Top row: XRF tomographic reconstructions for Murchison sample of Cr, Fe, Ni, and Zn $K\alpha$ fluorescence. Bottom row: XRD tomographic reconstruction of diffraction intensity at d -spacings of 7.2, 5.4, 6.0, 2.44, 1.77, and 1.56 Å.

XRF tomographic reconstructions of the Murchison sample are shown in Figure 11 (top row). As with MAC 88203, the Ca $K\alpha$ reconstruction is not shown due to the strong self-absorption effects so that only the outer ~ 50 μm of the fragment are well-resolved. However, several high Ca particles with diameters < 20 μm are visualized at the fragment edges. The Cr $K\alpha$ fluorescence intensity in the reconstruction is relatively uniform, except for several scattered isolated particles, typically < 15 μm in diameter, with moderate to high Cr $K\alpha$ intensities. Generally, the reconstructed fluorescence intensities of Fe, Ni, Zn, and Sr $K\alpha$ in the matrix do not vary significantly. There is an isolated ~ 100 μm diameter area in the upper left of the reconstruction that displays

lower fluorescence intensities for these four elements. Two smaller, isolated, high-Fe particles are noted at the top of the reconstruction near the fragment edge. The Ni, Zn, and Sr $K\alpha$ reconstructions are generally similar to the Fe reconstruction, with the exception that a number of small (< 15 μm diameter) high-Ni, and a few high-Zn and -Sr particles, are visible. The high-Ni particles generally do not correlate with the distribution of high-Cr particles.

The XRD tomographic reconstructions are shown in Figure 11 (middle and bottom row) for d -spacings of 7.2, 5.4, 6.0, 2.44, 1.77, and 1.56 Å. These reconstructions display notable heterogeneity in comparison to the XRF reconstructions, defining crystallographic differences that exist in the analyzed slice at micrometer scale. Iron-rich,

layer-lattice silicates are known to be a dominant mineral phase in most CM chondrites and in Murchison specifically (Barber, 1981; Brearley, 2014; Bunch & Chang, 1980; Fuchs et al., 1973; Howard et al., 2015; Mackinnon, 1980; Mackinnon & Buseck, 1979; Nakamura, 2005; Nakamura & Nakamuta, 1996; Suttle et al., 2021; Tomeoka & Buseck, 1985). These serpentine-group phyllosilicates are generally agreed to have formed by extensive aqueous alteration of the parent-body at low temperatures (Brearley, 2014; Nakamura, 2005). The reconstruction of the 7.2 Å reflection in Figure 11 shows high reconstructed intensity throughout the matrix and particularly strong reflections at the lower left corner of the reconstruction. On Figure 12, a reconstruction of diffraction intensity measured at 3.80 Å, the area in the lower left of the slice is defined as ROI-1. Higher intensities for the 7.2 Å reflection are also observed as rims on what are likely rounded chondrules and/or isolated mineral grains to the upper left (ROI-2) and upper right (ROI-3) of the slice. The integrated 2θ - I_{XRD} data for these three reconstructed ROIs are shown in Figure 13, along with the summed XRD pattern and caked area-detector frame for the entire fragment.

Iron-rich phyllosilicates are often the dominant mineral found in CM-type carbonaceous chondrites (Barber, 1981; Fuchs et al., 1973; Mackinnon, 1980; Nakamura, 2005), and previous X-ray diffraction studies of Murchison have identified the presence of three primary serpentine subgroups. Cronstedtite in Murchison shows a strong 001 basal reflection at 7.1–7.2 Å (Barber, 1981; Nakamura & Nakamuta, 1996) that is consistent with the 7.2 Å observed here in the XRD tomographic reconstruction of the fragment matrix (Figure 11) and particularly pronounced in the reconstructed $I_{\text{XRD}}(2\theta)$ of ROI-1 (Figure 13). The reconstructed $I_{\text{XRD}}(2\theta)$ of ROI-1 (Figure 13) also shows strong reflection intensities at 3.58 and 2.53 Å that are also consistent with cronstedtite. A calculated XRD pattern for cronstedtite is shown in Figure 14 for comparison. Note that in the summed XRD pattern for the whole fragment, the cronstedtite reflections at 7.2, 3.58, and 2.53 Å are the most intense and define smooth Debye–Scherrer rings, consistent with a fine-grained crystalline phase.

Tochilinite is also a commonly noted hydroxyl sulfide mineral in Murchison, which in previous XRD studies shows a strong 002 reflection at 5.4 Å and a very weak 001 reflection at 10.8 Å (Nakamura, 2005; Nakamura & Nakamuta, 1996). A 5.4 Å peak is noted in the XRD of the whole fragment (Figure 13) and is observed as strong intensity reflections in two areas (Figure 11) in the XRD tomographic reconstructions, one of which was defined as ROI-4 (Figure 12). A calculated XRD pattern for tochilinite is shown Figure 14 along with the reconstructed $I_{\text{XRD}}(2\theta)$ of ROI-4 for comparison.

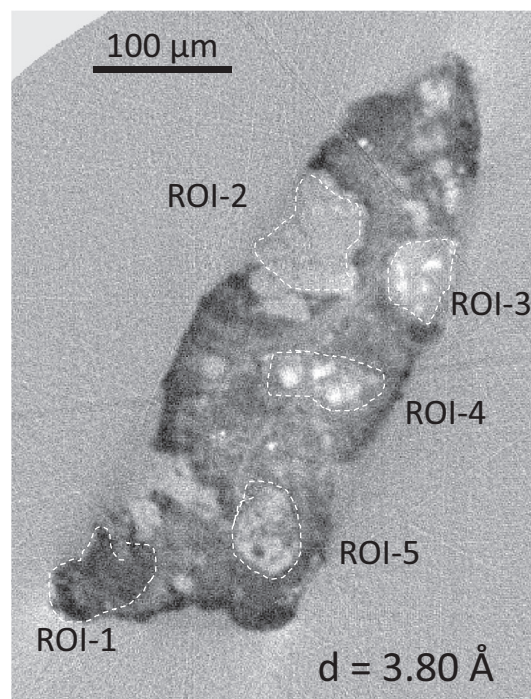


FIGURE 12. XRD tomographic reconstruction for Murchison sample at a d -spacing of 3.80 Å. Superimposed as dashed lines are five regions of interest (ROIs) from which integrated 2θ - I_{XRD} were calculated after tomographic reconstruction.

The reconstructed pattern for ROI-4 shows that the 5.4 Å peak dominates, but that lower intensity reflections from cronstedtite are also observed.

A related component that is commonly observed in Murchison and other CM2 chondrites are tochilinite–cronstedtite intergrowths (TCIs). These were referred to as poorly characterized phases (PCPs) in older literature (Fuchs et al., 1973; Mackinnon, 1980; Mackinnon & Buseck, 1979). The usage of the term PCP has been superseded in the recent literature by TCI to more accurately reflect the known characteristics of this component (King et al., 2019; Pignatelli et al., 2016; Suttle et al., 2021). These phases are known to consist of intergrowths of the Fe–Ni–S–O phase tochilinite and the Fe³⁺-rich serpentine cronstedtite, in various proportions (Nakamura, 2005; Nakamura & Nakamuta, 1996; Tomeoka & Buseck, 1985). In CM chondrites, these TCIs are hypothesized to have formed from progressive aqueous alteration and, in some, TCIs can constitute up to 30% by volume (Bunch & Chang, 1980). In XRD studies of TCIs in Murchison, strong reflections at 6.0 and 4.48 Å are also noted from a mixed-layer serpentine, in addition to reflections from cronstedtite and tochilinite (Nakamura & Nakamuta, 1996). This mixed-layer serpentine is presumed to be a secondary alteration

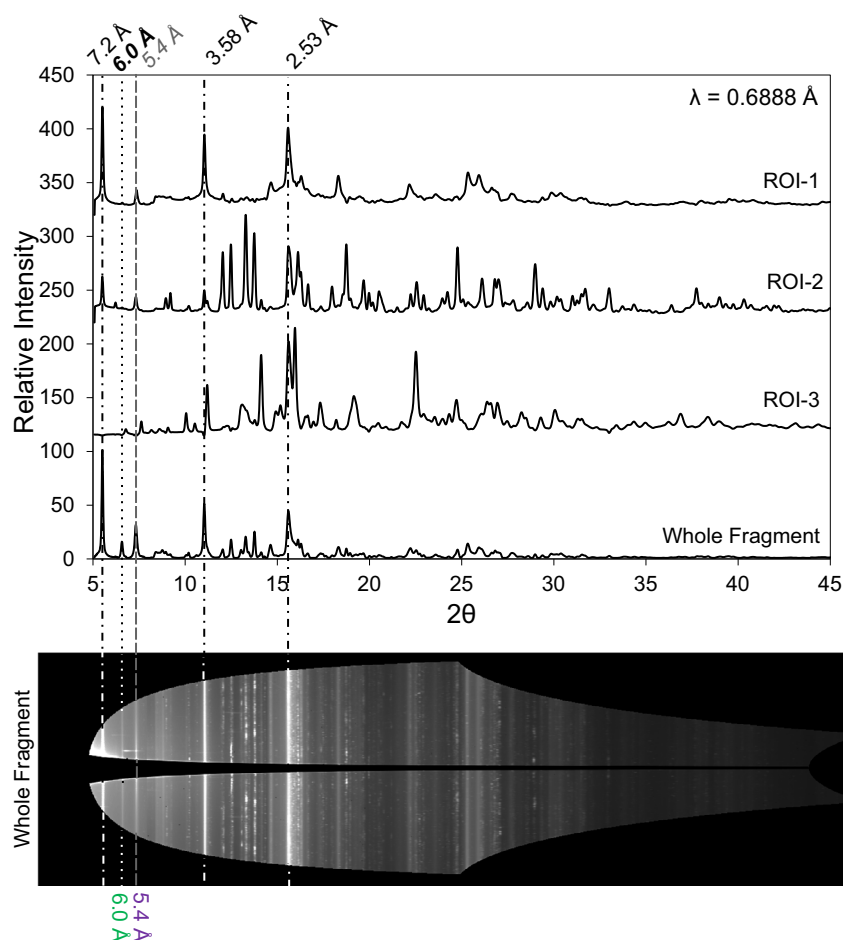


FIGURE 13. Integrated 99.9 percentile 2θ - I_{XRD} data for Murchison. Patterns are shown for the Whole Fragment (unreconstructed), and reconstructed patterns for the regions labeled ROI-1, ROI-2, and ROI-3 shown in Figure 12. The bottom image shows caked area-detector image for the entire fragment. The dashed lines show reference positions for high-intensity peaks for cronstedtite (dash-dot), tochilinite (dashed), and mixed-layer serpentine (dotted).

product of tochilinite. The 6.0 Å peak is noted in the XRD pattern of the whole Murchison fragment (Figure 13) and is observed in the tomographic reconstruction (Figure 11) as a strong localized reflection in the area designated ROI-5 (Figure 12). The reconstructed 2θ - I_{XRD} of ROI-5 in Figure 14 shows that the 6.0 Å peak dominates, but that the lower intensity reflection for the mixed-layer phase at 4.48 Å noted by Nakamura and Nakamura (1996) is also observed, as are lower intensity reflections from cronstedtite and tochilinite.

The XRD reconstruction for ROI-2, which is characterized by lower Fe fluorescence relative to the matrix in the XRF reconstruction, shows the presence of scattered isolated particles in this area with diffraction consistent with a clinoenstatite-type structure (Figure 13). These are best visualized by the reconstruction of the 2.44 Å reflection (Figure 11). The spherical area defined by ROI-3, however, shows Fe fluorescence intensities comparable to that observed in the matrix. This area is

best visualized by the reconstruction of the 1.77 Å reflection (Figure 11) and the reconstructed 2θ - I_{XRD} for ROI-3 is consistent with olivine of largely forsteritic composition. If the rounded isolated particles defined by ROI-2 and ROI-3 are chondrules, then ROI-2 may be most consistent with a pyroxene-rich type IB chondrule, while ROI-3 may be consistent with a type IA, which are dominated by forsteritic olivine (Hewins, 1997; McSween Jr, 1977). A reconstruction of diffraction intensity at 1.56 Å (Figure 11) shows an intense reflection from an isolated mineral grain immediately adjacent to ROI-3, with diffraction pattern consistent with low Fe spinel, noting that the XRF reconstruction also suggests that Fe abundance is low. The presence of low FeO spinels in Murchison has been previously noted (Kuehner & Grossman, 1987).

As with MAC 88203, following initial assessment of the XRF/XRD tomographic reconstruction, the fiber-mounted Murchison fragment was epoxy embedded to

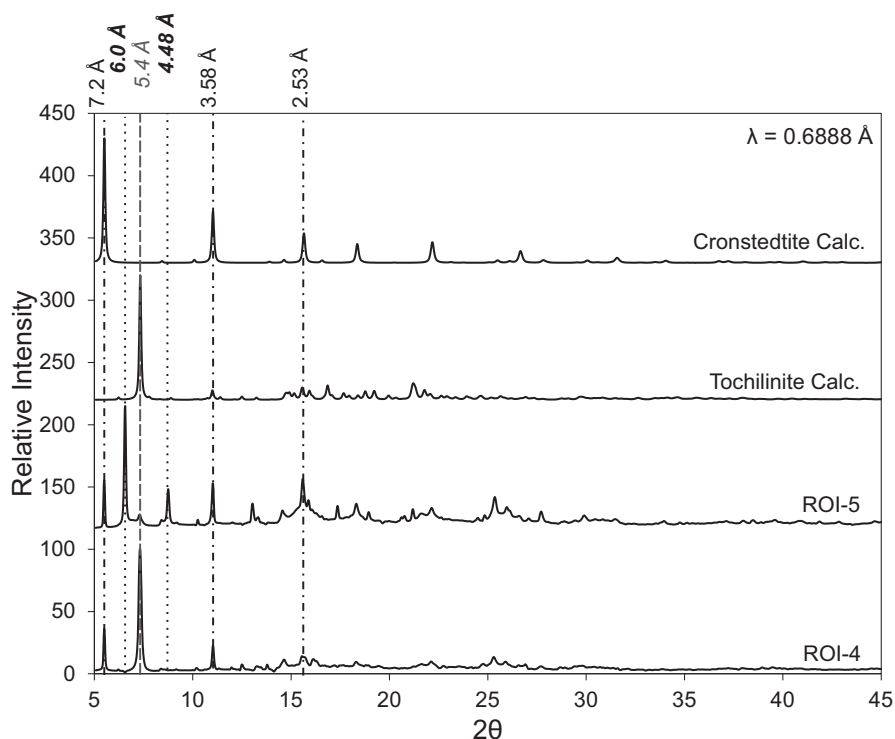


FIGURE 14. Reconstructed 99.9 percentile 2θ - I_{XRD} data for Murchison regions labeled ROI-4 and ROI-5 in comparison to calculated XRD patterns for cronstedtite and tochilinite. The lines show reference positions for high-intensity peaks for cronstedtite (dash-dot), tochilinite (dashed), and mixed-layer serpentinite (dotted).

produce a singly polished section for SEM analysis. Figure 15 shows a BSE image (upper left) of this section, along with energy-dispersive maps of Fe, Mg, and S K-fluorescence. The SEM imaging shows the presence of three rounded isolated clinoenstatite-rich particles ($\sim\text{Fs}_3$), consistent with being pyroxene-rich type IB chondrules. The chondrule in the upper right of the section is the most notable and includes a large grain of metallic Fe. Less abundant are isolated olivine grains, with a relatively large olivine observable in the upper left of the section. The relative distribution of scattered clinoenstatite and olivine crystals in the section is consistent with the interpretations made from the XRF/XRD tomography analysis, although no metallic Fe phases were observed in the tomographic data set. The matrix mineralogy of the SEM section is dominated by high-Fe serpentine-group phase, again, consistent with the interpretations made from the XRF/XRD tomography. Also identified in the SEM section are disseminated particles between ~ 10 and $50\ \mu\text{m}$ in diameter that are enriched in Fe, Ni, S, and O that are likely TCI grains, the largest of which is designated in Figure 15. This is consistent with the observations made from the XRD tomographic analysis for this fragment. Overall, the mineralogy of this Murchison fragment is

expected based on previous descriptions of the meteorite (Fuchs et al., 1973; Metzler et al., 1992).

IMPLICATIONS

Combined XRF and XRD tomography results are presented from three compositionally diverse chondritic meteorite samples, including samples prepared from fragments of CR2, H5, and CM2 chondrites. In all three cases, the mineralogy inferred based on the tomographic reconstructions of XRF spectral and XRD reflection intensities is consistent with mineralogy established from previously reported petrographic information and from the post-tomography electron microscope analysis for each of the three meteorites. For sample LAP 02342, a CR2 chondrite prepared as an epoxy embedded mount from crushed material, the primary mineral phases that were identified included isolated grains of α -Fe and likely some intermixed coarsely crystalline enstatite and olivine. There is a possibility that some reflections are from gehlenite, but this is not definitive. The imaged mineralogy is generally consistent with reported petrographic information for LAP 02342 (Righter & Satterwhite, 2004), which note abundant metal and pyroxene. FeO-rich phyllosilicates that have been

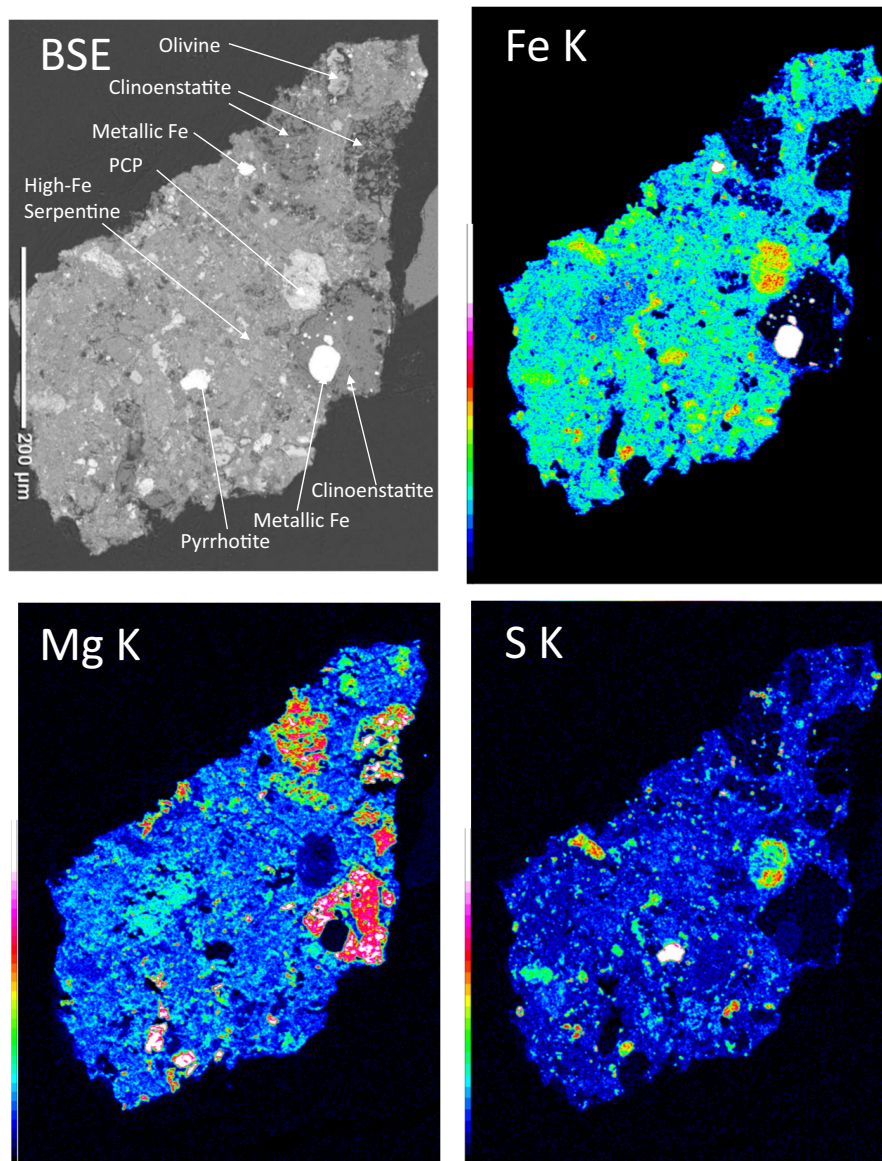


FIGURE 15. BSE image (upper left) and SEM energy-dispersive maps of Fe, Mg, and S K-fluorescence for epoxy embedded polished section of Murchison sample. Representative phases identified using electron microscopy are noted on the BSE image. Relative fluorescence intensity scales are shown for the energy-dispersive maps.

reported as a major matrix mineral were not identified. However, given that this sample was ground in preparation, it is likely that grinding has biased the preserved mineralogy so that more mechanically robust phases are preferentially represented in the epoxy mount.

The samples of the H5 chondrite MAC 88203 and CM2 Murchison, however, were analyzed as whole, unsectioned samples between 300 and 400 µm in diameter. For these analyses, the spatial relationships between mineral grains are preserved, including fine-grained matrix phases. In the H5 chondrite sample, MAC 88203, XRF/XRD tomography identifies forsteritic

olivine as a primary mineral phase and was able to clearly visualize a fusion crust at the sample surface. Although uniquely constraining the composition of the fusion crust from the tomographic XRF and XRD data were not possible, the data did show that the X-ray scattering from the material is consistent with an olivine structure. A diffuse olivine pattern may be reasonable for vitrified fusion crust in this case. Small, localized Cr-rich spinels were also identifiable at spatial resolutions of several micrometers. However, the tomographic data did not allow for clear identification of matrix oligoclase crystals that are visible in SEM images of the MAC 88203

sample. The tomographic reconstruction of 2θ - I_{XRD} data for areas defined as “matrix” in the reconstructed slice is the most consistent with olivine, rather than plagioclase. However, if the plagioclase-rich matrix is glassy, as might be expected for maskelynite, it is possible that the diffuse scattering does not yield strong reflections relative to the diffraction from small olivine crystallites that may be present.

In the Murchison CM2 chondrite sample, major identifiable phases include clinoenstatite- and olivine-rich chondrules and serpentine matrix minerals. Small Cr-rich spinels also are identifiable. These are all phases that are consistent with prior studies of Murchison and with the post-tomographic SEM imaging conducted here. Most notable in our tomographic analysis of Murchison is that the technique can quantitatively distinguish and visualize the complex mixture of serpentine-group minerals and associated TCI that are present.

In the three samples evaluated, XRF/XRD tomography provides unique mineral identifications for most major phases observed, which here include metallic phases, olivine and pyroxene phenocrysts, and phyllosilicate matrix phases. Generally, the XRD image reconstructions allows for visualization of differences in mineralogy and crystal structures at spatial resolutions of 1–2 μm , the pixel size of the fast-scanning motor and focus size of the incident beam used for these experiments. Line artifacts in the XRD reconstructions, arising primarily from large crystallites in the sample where repeated crystal units satisfy the Bragg condition, can be suppressed through intensity filtering prior to reconstruction, but cannot be eliminated using this approach. Minor phases with particle sizes <15 μm diameter, such as spinels, can be identifiable with moderate confidence. The XRD tomographic reconstruction of 2θ - I_{XRD} for these small particles often include intensity contributions from surrounding crystalline phases, which makes equivocal identification based on the XRD data alone more difficult. However, combination with the tomographic reconstruction of the XRF intensities, which are collected simultaneously, narrows the range of likely phases. Such correlation of XRD and XRF intensities is more difficult for solid meteoritic samples that are 300 μm in diameter or larger due to self-absorption effects, which strongly attenuate low-energy XRF emissions. Similarly, poorly crystalline phases, particularly in the matrix, may also see intensity contributions from surrounding crystalline phases.

The XRD tomographic reconstructions can be computationally intensive. In this study, the individual calibrated 2-D area detector frames were azimuthally integrated to 1-D arrays of 2θ angle versus diffraction intensity, from which summed 2θ ranges are then extracted for tomographic reconstruction, which is

computationally efficient. However, with improved computational hardware, future studies will allow for integrating the diffraction signal along the azimuthal angle and for subsets of the pixel array (i.e., potential locations of Bragg reflections) that can then be correlated with 2θ , ω , and the azimuthal and radial in-plane detector angles χ and θ . This can provide sets of single crystal reflections for phases that give no powder-like diffraction signal at the given spatial scale of the focused beam, here $1 \times 2 \mu\text{m}$. It will also be possible with new computational resources to reconstruct 2-D area-detector images for each voxel rather than just 1-D 2θ - I_{XRD} . This requires tomographic reconstruction of intensity measured in each pixel of the area detector, which for the Eiger 1 M detector used here is 1028×1062 pixels. Although computationally intensive, this would allow for the better evaluation of the contribution to the measured diffraction of individual components in complex mixtures.

For studying extraterrestrial samples, whether meteorite fragments or materials from sample return missions, this analytical approach can provide researchers a primary evaluation of grain sizes, mineral texture, modal abundances, preferred orientation, void space, etc. For irreplaceable samples, this can be a powerful method for pre-screening prior to analysis by other techniques that result in material loss either during sample preparation or as part of the analysis itself. The penetration provided by X-rays at incident energies >16 keV provides significant flexibility in sample mounting. Here, fragments were epoxy mounted to silica fibers, with the primary mounting consideration being that samples can be precisely centered with respect to the incident focused beam and the rotation center of the stage using a goniometer and that any encasing media has relatively low X-ray attenuation. Thus, samples encased in low attenuation capillaries or containers can feasibly be interrogated. Although low-energy fluorescence X-rays are strongly self-absorbed during analysis, X-ray diffraction intensities are equal to the energy of the incident beam such that at incident beam energies >18 keV it is feasible to collect XRD tomographic data on silicate samples hundreds of micrometers in diameter.

The high flux and small source size available at third and fourth generation synchrotron facilities can allow X-ray microprobes to make these types of XRF and XRD tomographic measurements with micrometer and sub-micrometer spatial resolutions, without requirements for sample sectioning, analysis in vacuum or sample coating. However, it is still important to consider that the radiation dose delivered to the analyzed slices is significant. In the analyses presented here, between 1×10^8 and 1×10^9 Gy is delivered along the analyzed tomographic slice, and this irradiation can potentially alter some sample characteristics along the irradiated portion of the sample. For example, full-field synchrotron

X-ray microcomputed tomography has been shown to alter the natural radiation record preserved in some extraterrestrial samples (Sears et al., 2018) and a number of X-ray absorption spectroscopy studies with synchrotron microprobe beams have shown that the speciation of some elements in some natural glasses and minerals can alter during analysis, particularly if the materials are hydrated (i.e., Cottrell et al., 2018). In contrast, full-field tomographic imaging of CM chondrites with doses of monochromatic and polychromatic radiation up to 3 kiloGray (kGy) have found no differences in the amino acid abundances and negligible sample heating due to X-ray exposure (Friedrich et al., 2016, 2019). What is apparent in the analyses presented as part of this study is that the mineral phases identified, including olivines, pyroxenes, metals and metal oxides, serpentine-group minerals, and associated TCIs, show no detectable changes in diffraction peak positions or resolution over the course of the analysis. These would be expected to be indicators for radiation-induced changes in mineral structure. In addition, the use of a highly focused X-ray beam, in these analyses using a beam focused to 1 μm in the vertical, means that the majority of sample and areas immediately adjacent to the interrogated slice have not been impacted by potential irradiation effects and can easily be avoided during subsequent analysis and sampling. As such, this approach may be particularly useful as a pre-screening analytical measurement for valuable extraterrestrial materials that can provide quantitative mineralogical and chemical characterization at a micrometer scale. This can be particularly useful for spacecraft sample returns, samples which are generally small enough to be amenable to the techniques.

Acknowledgments—US Antarctic meteorite samples are recovered by the Antarctic Search for Meteorites (ANSMET) program, which has been funded by NSF and NASA and characterized and curated by the Department of Mineral Sciences of the Smithsonian Institution and the Astromaterials Curation Office at the NASA Johnson Space Center. This work was supported by a grant to the University of Chicago (subaward to the University of New Mexico) from the NASA Laboratory Analysis of Returned Samples program (80NSSC18K0500 and 80NSSC21K0611). Portions of this work were performed at GeoSoilEnviroCARS (The University of Chicago, Sector 13), Advanced Photon Source (APS), Argonne National Laboratory. GeoSoilEnviroCARS is supported by the National Science Foundation—Earth Sciences (EAR – 1634415) and NASA’s Planetary Major Enabling Facilities (PSEF) program (grant number 80NSSC23K0196) and NASA 80HQTR20T0014 (SSERVI RISE2). This research used resources of the Advanced Photon Source, a U.S. Department of Energy (DOE) Office of Science User Facility operated for the DOE Office of

Science by Argonne National Laboratory under Contract No. DE-AC02-06CH11357. The authors also wish to thank Scott Sanford, for editorial handling of this manuscript, and George Flynn and Allan Treiman for their insightful reviews which significantly improved the final manuscript.

Data Availability Statement—The data that support the findings of this study are available from the corresponding author upon reasonable request.

Editorial Handling—Dr. Scott Sandford

REFERENCES

- Adcock, C., Tschauer, O., Hausrath, E. M., Udry, A., Luo, S.-N., Cai, Y., Ren, M., Lanzirotti, A., et al. 2017. Shock-Transformation of Whitlockite to Merrillite and the Implications for Planetary Water Budgets. *Nature Communications* 8: 14667.
- Alvarez-Murga, M., Bleuët, P., and Hodeau, J.-L. 2012. Diffraction/Scattering Computed Tomography for Three-Dimensional Characterization of Multi-Phase Crystalline and Amorphous Materials. *Journal of Applied Crystallography* 45: 1109–24.
- Alvarez-Murga, M., Bleuët, P., Marques, L., Lepoittevin, C., Boudet, N., Gabarino, G., Mezouar, M., and Hodeau, J.-L. 2011. Microstructural Mapping of C60 Phase Transformation into Disordered Graphite at High Pressure, Using X-Ray Diffraction Microtomography. *Journal of Applied Crystallography* 44: 163–171.
- Artioli, G., Cerulli, T., Cruciani, G., Dalconi, M., Ferrari, G., Parisatto, M., Rack, A., and Tucoulou, R. 2010. X-Ray Diffraction Microtomography (XRD-CT), a Novel Tool for Non-invasive Mapping of Phase Development in Cement Materials. *Analytical and Bioanalytical Chemistry* 397: 2131–36.
- Ashiotis, G., Deschildre, A., Nawaz, Z., Wright, J. P., Karkoulis, D., Picca, F. E., and Kieffer, J. 2015. The Fast Azimuthal Integration Python Library: pyFAI. *Journal of Applied Crystallography* 48: 510–19.
- Barber, D. J. 1981. Matrix Phyllosilicates and Associated Minerals in C2M Carbonaceous Chondrites. *Geochimica et Cosmochimica Acta* 45: 945–970.
- Bland, P. A., Zolensky, M. E., Benedix, G. K., and Sephton, M. A. 2006. Weathering of Chondritic Meteorites. In *Meteorites and the Early Solar System II*, edited by D. S. Lauretta, and H. Y. McSween, 853–868. Arizona: University of Arizona Press.
- Bleuët, P., Welcomme, E., Dooryhee, E., Susini, J., Hodeau, J.-L., and Walter, P. 2008. Probing the Structure of Heterogeneous Diluted Materials by Diffraction Tomography. *Nature Materials* 7: 468–472.
- Brearley, A. 2014. Nebular Versus Parent Body Processing. In *Meteorites and Cosmochemical Processes, Volume 1 of Treatise on Geochemistry*, edited by A. M. Davis, 2nd ed., 309–334. Amsterdam: Elsevier.
- Bunch, T., and Chang, S. 1980. Carbonaceous Chondrites—II. Carbonaceous Chondrite Phyllosilicates and Light Element Geochemistry as Indicators of Parent Body Processes and Surface Conditions. *Geochimica et Cosmochimica Acta* 44: 1543–77.

- Cottrell, E., Lanzirrotti, A., Mysen, B., Birner, S., Kelley, K., Botcharnikov, R., Davis, F., and Newville, M. 2018. A Mössbauer-Based XANES Calibration for Hydrous Basalt Glasses Reveals Radiation-Induced Oxidation of Fe. *American Mineralogist* 103: 489–501.
- Dong, H., Butler, K. T., Matras, D., Price, S. W. T., Odarchenko, Y., Khatry, R., Thompson, A., et al. 2021. A Deep Convolutional Neural Network for Real-Time Full Profile Analysis of Big Powder Diffraction Data. *NPJ Computational Materials* 7: 74.
- Dowd, B. A., Campbell, G. H., Marr, R. B., Nagarkar, V. V., Tipnis, S. V., Axe, L., and Siddons, D. P. 1999. Developments in Synchrotron X-Ray Computed Microtomography at the National Synchrotron Light Source. *International Society for Optics and Photonics*. 3772: 224–236.
- Ebel, D. S., and Rivers, M. L. 2007. Meteorite 3-D Synchrotron Microtomography: Methods and Applications. *Meteoritics & Planetary Science* 42: 1627–46.
- Eckley, S. A., and Ketcham, R. A. 2022. The Utility of X-Ray Computed Tomography in Astromaterials Research and Curation: A Case Study from Martian Meteorites. *Microscopy and Microanalysis* 28: 2678–80.
- El Goresy, A., and Fechtig, H. 1967. Fusion Crust of Iron Meteorites and Mesosiderites and Production of Cosmic Spherules. *Smithsonian Contributions to Astrophysics* 11: 391.
- Flynn, G., Sutton, S., and Lanzirrotti, A. 2009. A Synchrotron-Based Facility for the In-Situ Location, Chemical and Mineralogical Characterization of 10 μm Particles Captured in Aerogel. *Advances in Space Research* 43: 328–334.
- Friedrich, J. M., Glavin, D. P., Rivers, M. L., and Dworkin, J. P. 2016. Effect of a Synchrotron X-Ray Microtomography Imaging Experiment on the Amino Acid Content of a CM Chondrite. *Meteoritics & Planetary Science* 51: 429–437.
- Friedrich, J. M., McLain, H. L., Dworkin, J. P., Glavin, D. P., Towbin, W. H., Hill, M., and Ebel, D. S. 2019. Effect of Polychromatic X-Ray Microtomography Imaging on the Amino Acid Content of the Murchison CM Chondrite. *Meteoritics & Planetary Science* 54: 220–28.
- Fuchs, L. H., Olsen, E., and Jensen, K. J. 1973. Mineralogy, Mineral-Chemistry, and Composition of the Murchison (C2) Meteorite. In *Smithsonian Contributions to the Earth Sciences 10*. Washington: Smithsonian Institution Press.
- Genge, M. J., Alesbrook, L., Almeida, N., Bates, H., Bland, P., Boyd, M., Burchell, M., et al. 2023. The Fusion Crust of the Winchcombe Meteorite: A Preserved Record of Atmospheric Entry Processes. *Meteoritics & Planetary Science*: 13937. <https://doi.org/10.1111/maps.13937>
- Genge, M. J., and Grady, M. M. 1999. The Fusion Crusts of Stony Meteorites: Implications for the Atmospheric Reprocessing of Extraterrestrial Materials. *Meteoritics & Planetary Science* 34: 341–356.
- Gräfe, M., Klauber, C., Gan, B., and Tappero, R. V. 2014. Synchrotron X-Ray Microdiffraction (μXRD) in Minerals and Environmental Research. *Powder Diffraction* 29: S64–S72.
- Grant, J., Morgan, M., Davis, J., Davies, D., and Wells, P. 1993. X-Ray Diffraction Microtomography. *Measurement Science and Technology* 4: 83–87.
- Grossman, J. N., and Score, R. 1996. The Meteoritical Bulletin, No. 79, 1996 July: Recently Classified Specimens in the United States Antarctic Meteorite Collection (1994–1996). *Meteoritics & Planetary Science* 31: A161–A174.
- Gürsoy, D., Biçer, T., Lanzirrotti, A., Newville, M. G., and De Carlo, F. 2015. Hyperspectral Image Reconstruction for X-Ray Fluorescence Tomography. *Optics Express* 23: 9014–23.
- Gürsoy, D., De Carlo, F., Xiao, X., and Jacobsen, C. 2014. TomoPy: A Framework for the Analysis of Synchrotron Tomographic Data. *Journal of Synchrotron Radiation* 21: 1188–93.
- Hewins, R. H. 1997. Chondrules. *Annual Review of Earth and Planetary Sciences* 25: 61–83.
- Howard, K., Alexander, C. O., Schrader, D. L., and Dyl, K. 2015. Classification of Hydrous Meteorites (CR, CM and C2 Ungrouped) by Phyllosilicate Fraction: PSD-XRD Modal Mineralogy and Planetsimal Environments. *Geochimica et Cosmochimica Acta* 149: 206–222.
- Kayama, M., Tomioka, N., Ohtani, E., Seto, Y., Nagaoka, H., Götz, J., Miyake, A., et al. 2018. Discovery of Moganite in a Lunar Meteorite as a Trace of H_2O Ice in the Moon's Regolith. *Science Advances* 4: eaar4378.
- Keller, L. P., Thomas, K. L., and McKay, D. S. 1992. Thermal Processing of Cosmic Dust: Atmospheric Heating and Parent Body Metamorphism. *23rd Lunar and Planetary Science Conference*, p. 675.
- King, A., Russell, S., Schofield, P., Humphreys-Williams, E., Strekopytov, S., Abernethy, F., Verchovsky, A., and Grady, M. 2019. The Alteration History of the Jbilet Winselwan CM Carbonaceous Chondrite: An Analog for C-Type Asteroid Sample Return. *Meteoritics & Planetary Science* 54: 521–543.
- Kuehner, S. M., and Grossman, L. 1987. Petrography and Mineral Chemistry of Spinel Grains Separated from the Murchison Meteorite In *Abstracts of the Lunar and Planetary Science Conference*, vol. 18, p. 519.
- Lange, K., Rowe, R., Jamieson, H., Flemming, R., and Lanzirrotti, A. 2010. Characterization of Geosynthetic Clay Liner Bentonite Using Micro-Analytical Methods. *Applied Geochemistry* 25: 1056–69.
- Lanzirrotti, A., Tappero, R., and Schulze, D. G. 2010. Chapter 2—Practical Application of Synchrotron-Based Hard X-Ray Microprobes in Soil Sciences. In *Developments in Soil Science*, edited by B. Singh, and M. Gräfe, 27–72. Amsterdam: Elsevier.
- Le Guillou, C., Changela, H. G., and Brearley, A. J. 2015. Widespread Oxidized and Hydrated Amorphous Silicates in CR Chondrites Matrices: Implications for Alteration Conditions and H_2 Degassing of Asteroids. *Earth and Planetary Science Letters* 420: 162–173.
- Ma, C., Tschauner, O., Beckett, J. R., Rossman, G. R., and Liu, W. 2012. Panguite, $(\text{Ti}^{4+}, \text{Sc}, \text{Al}, \text{Mg}, \text{Zr}, \text{Ca})_{1.8}\text{O}_3$, a New Ultra-Refractory Titania Mineral from the Allende Meteorite: Synchrotron Micro-Diffraction and EBSD. *American Mineralogist* 97: 1219–25.
- Mackinnon, I. D. 1980. Structures and Textures of the Murchison and Mighei Carbonaceous Chondrite Matrices In: 11th Lunar and Planetary Science Conference, Houston, TX, March 17–21, Proceedings. Volume 2 (A82-22296 09-91). New York, Pergamon Press, pp. 839–52.
- Mackinnon, I. D. R., and Buseck, P. R. 1979. New Phyllosilicate Types in a Carbonaceous Chondrite Matrix. *Nature* 280: 219–220.

- Marlow, R., Satterwhite, C., and Mason, B. 1994. Antarctic Meteorite Newsletter, volume 17, Number 3. 27.
- McSween, H. Y., Jr. 1977. On the Nature and Origin of Isolated Olivine Grains in Carbonaceous Chondrites. *Geochimica et Cosmochimica Acta* 41: 411–18.
- Metzler, K., Bischoff, A., and Stöffler, D. 1992. Accretionary Dust Mantles in CM Chondrites: Evidence for Solar Nebula Processes. *Geochimica et Cosmochimica Acta* 56: 2873–97.
- Miyahara, M., Kaneko, S., Ohtani, E., Sakai, T., Nagase, T., Kayama, M., Nishido, H., and Hirao, N. 2013. Discovery of Seifertite in a Shocked Lunar Meteorite. *Nature Communications* 4: 1737.
- Nakamura, T. 2005. Post-Hydration Thermal Metamorphism of Carbonaceous Chondrites. *Journal of Mineralogical and Petrological Sciences* 100: 260–272.
- Nakamura, T., and Nakamura, Y. 1996. X-Ray Study of PCP from the Murchison CM Carbonaceous Chondrite, p. 37. Newville, M. 2013. Larch: An Analysis Package for XAFS and Related Spectroscopies. *Journal of Physics: Conference Series* 430: 012007.
- Pignatelli, I., Marrocchi, Y., Vacher, L. G., Delon, R., and Gounelle, M. 2016. Multiple Precursors of Secondary Mineralogical Assemblages in CM Chondrites. *Meteoritics & Planetary Science* 51: 785–805.
- Possenti, E., Conti, C., Gatta, G. D., Marinoni, N., Merlini, M., Realini, M., Vaughan, G. B., and Colombo, C. 2022. Synchrotron X-Ray Diffraction Computed Tomography to Non-Destructively Study Inorganic Treatments for Stone Conservation. *Iscience* 25: 105112.
- Prescher, C., and Prakapenka, V. B. 2015. DIOPTAS: A Program for Reduction of Two-Dimensional X-Ray Diffraction Data and Data Exploration. *High Pressure Research* 35: 223–230.
- Righter, K., and Satterwhite, C. 2004. Antarctic Meteorite Newsletter, volume 27, number 27.
- Russell, S. S., Zolensky, M., Righter, K., Folco, L., Jones, R., Connolly, H. C., Jr., Grady, M. M., and Grossman, J. N. 2005. The Meteoritical Bulletin, no. 89. *Meteoritics & Planetary Science* 40: A201–A263.
- Sears, D. W., Sehlke, A., Friedrich, J. M., Rivers, M. L., and Ebel, D. S. 2018. X-Ray Computed Tomography of Extraterrestrial Rocks Eradicates their Natural Radiation Record and the Information it Contains. *Meteoritics & Planetary Science* 53: 2624–31.
- Suttle, M., King, A., Schofield, P., Bates, H., and Russell, S. 2021. The Aqueous Alteration of CM Chondrites, a Review. *Geochimica et Cosmochimica Acta* 299: 219–256.
- Sutton, S. R., Lanzirotti, A., Newville, M., Rivers, M. L., Eng, P., and Lefticariu, L. 2017. Spatially Resolved Elemental Analysis, Spectroscopy and Diffraction at the GSECARS Sector at the Advanced Photon Source. *Journal of Environmental Quality* 46: 1158–65.
- Tomeoka, K., and Buseck, P. R. 1985. Indicators of Aqueous Alteration in CM Carbonaceous Chondrites: Microtextures of a Layered Mineral Containing Fe, S, O and Ni. *Geochimica et Cosmochimica Acta* 49: 2149–63.
- Tschauner, O., Huang, S., Yang, S., Humayun, M., Liu, W., Gilbert, C. S. N., Bechtel, H. A., Tischler, J., and Rossman, G. R. 2021. Discovery of Davemaoite, CaSiO₃-Perovskite, as a Mineral from the Lower Mantle. *Science* 374: 891–94.
- Tschauner, O., Ma, C., Lanzirotti, A., and Newville, M. G. 2020. Riesite, a New High Pressure Polymorph of TiO₂ from the Ries Impact Structure. *Minerals* 10: 78.
- Tschauner, O., Ma, C., Newville, M. G., and Lanzirotti, A. 2020. Structure Analysis of Natural Wangdaodeite—LiNbO₃-Type FeTiO₃. *Minerals* 10: 1072.
- Vamvakeros, A., Jacques, S. D., Di Michiel, M., Middelkoop, V., Egan, C. K., Cernik, R. J., and Beale, A. M. 2015. Removing Multiple Outliers and Single-Crystal Artefacts from X-Ray Diffraction Computed Tomography Data. *Journal of Applied Crystallography* 48: 1943–55.
- Walker, S. R., Parsons, M. B., Jamieson, H. E., and Lanzirotti, A. 2009. Arsenic Mineralogy of Near-Surface Tailings and Soils Determined by Synchrotron Micro-Probe and Petrographic Methods: Controls on Arsenic Behaviour and Bioaccessibility in the Nova Scotia Gold Mining Districts. *Canadian Mineralogist* 47: 533–556.
- Wasson, J. T., and Rubin, A. E. 2009. Composition of Matrix in the CR Chondrite LAP 02342. *Geochimica et Cosmochimica Acta* 73: 1436–60.
- Weisberg, M. K., Prinz, M., Clayton, R. N., and Mayeda, T. K. 1993. The CR (Renazzo-Type) Carbonaceous Chondrite Group and its Implications. *Geochimica et Cosmochimica Acta* 57: 1567–86.
- Zeigler, R., Gross, J., Eckley, S., and McCubbin, F. 2022. Using X-Ray Computed Tomography to Catalog Rock Fragments in Apollo Drive Tube 73002.